

A MIXED FINITE VOLUME ELEMENT METHOD
FOR ACCURATE COMPUTATION OF FLUID
VELOCITIES IN POROUS MEDIA

by

Jim E. Jones

B.S., New Mexico Tech, 1986

M.S., New Mexico Tech, 1989

A thesis submitted to the
Faculty of the Graduate School of the
University of Colorado at Denver
in partial fulfillment
of the requirements for the degree of
Doctor of Philosophy
Applied Mathematics
1995

This thesis for the Doctor of Philosophy

degree by

Jim E. Jones

has been approved

by

Stephen F. McCormick

Thomas A. Manteuffel

John W. Ruge

Thomas F. Russell

John Trapp

Date

Jones, Jim E. (Ph.D., Applied Mathematics)

A Mixed Finite Volume Element Method for Accurate Computation of
Fluid Velocities in Porous Media

Thesis directed by Professor Stephen F. McCormick

ABSTRACT

A key ingredient in the simulation of flow in porous media is the accurate determination of the velocities that drive the flow. Large-scale irregularities of the geology, such as faults, fractures, and layers, suggest the use of irregular grids in the simulation. In this study, the approach to this problem was to apply the finite volume element methodology, developed by McCormick, in conjunction with mixed methods, developed by Raviart and Thomas. The resulting mixed finite volume element discretization scheme developed here can be applied in a clear and straightforward way to irregular grids and is appealing because of its local conservation properties and its direct and accurate representation of physical intercell flux terms. Several multilevel algorithms are developed that provide efficient methods for solving the set of equations that this discretization produces. This thesis includes numerical results from a variety of test problems, from Poisson's equation to problems with anisotropic, discontinuous, and tensor diffusion coefficients. These

results show that this approach has the potential to generate accurate approximate fluid velocities and that the multilevel methods can provide fast solvers.

This abstract accurately represents the content of the candidate's thesis. I recommend its publication.

Signed

Stephen F. McCormick

Contents

Chapter

1 Uniform Grids 1

1.1 The Mixed Finite Volume Element Discretization 1

1.2 An FVE Based Multigrid Algorithm 13

1.2 Computational Results 25

1.2.1 Comparison to Finite Differences for Poisson Problem ... 25

1.2.2 Discontinuous and Anisotropic Diffusion Coefficients 30

1.2.3 An Alternative Multilevel Algorithm 35

1.2.4 Full Tensor Diffusion Coefficients 42

Chapter

2 General Quadrilateral Grids 46

2.1 The Mixed FVE Discretization 46

2.2 Multilevel Solvers 55

2.2.1 FVE Based Multigrid 55

2.2.2 A Two-Level Approach 60

2.3 Computational Results 62

2.3.1 Multigrid Performance 62

2.3.2 Two-Level Performance	67
2.3.3 Accuracy of the Mixed FVE Discretization	70
<u>Chapter</u>	
3 Technical Derivations	77
3.1 Uniform Grids and Tensor Permeability	77
3.2 Derivation of FVE Stencils for General Quadrilaterals	80
3.2.1 Scalar Diffusion Coefficient	80
3.2.2 Tensor Diffusion Coefficient	89
3.3 Using Fine Grid Integrals to Calculate Coarse Grid Integrals	91
<u>Chapter</u>	
4 Summary and Future Work	97
<u>Bibliography</u>	100

ACKNOWLEDGEMENTS

This thesis presents the results from a five-year period of research, and it would not be complete without a word of special thanks to those whose assistance enabled me to complete it.

First of all, I wish to thank Professor Steve McCormick for giving me the opportunity to work on a host of interesting research projects. I also thank Professor McCormick for the wide freedom that I was given as a graduate student to do independent research, and his patience as I labored to bring this research to its conclusion.

I also wish acknowledge Professor Thomas Russell for his assistance with this work. Without his expertise in the field of reservoir simulation, this research could not have taken place. I also wish to thank Professor John Ruge and Professor Steve Schaffer. While they were not directly involved in the day-to-day work on this project, I learned most of what I know about multigrid methods through collaborative research with these two men.

I would also like to thank Dr. Pat Roache, Ecodynamics Research, and Sandia National Laboratory for their financial support at various times during this research.

Finally, I wish to acknowledge the countless sacrifices made by my family - my wife Dorothee, my daughter Frederika, and my yet un-named second child - that allowed me to complete this thesis. Most of all I thank my wife for her unfailing love and support during this time.

1 Uniform Grids

1.1 The Mixed Finite Volume Element Discretization

In this first section, we introduce the new mixed finite volume element discretization technique in a familiar context: solving the diffusion equation on a uniform, square grid. However, it should be clear from the presentation that the discretization developed in this section, and the multigrid algorithm constructed in the next section, can easily be modified to apply to any tensor product grid.

We begin by considering the following partial differential equation defined on some square coordinate-aligned domain Ω in \mathcal{R}^2 :

$$\begin{cases} -\nabla \cdot \mathbf{A}(\mathbf{x})\nabla\phi(\mathbf{x}) = f(\mathbf{x}), & \mathbf{x} \in \Omega, \\ \mathbf{A}(\mathbf{x})\nabla\phi(\mathbf{x}) \cdot \boldsymbol{\eta} = g(\mathbf{x}), & \mathbf{x} \in \partial\Omega. \end{cases} \quad (1.1)$$

In the context of reservoir simulation, this is the pressure equation for incompressible single-phase flow, where ϕ is the pressure in the reservoir Ω and the boundary condition specifies the flux on $\partial\Omega$. Because one of our

goals for the new discretization is accurate approximations of flow velocities, we will begin by reformulating this equation as a first-order system of equations, where velocity appears explicitly. This is done by introducing the flow velocity variables via the definition

$$\mathbf{v} \equiv -\mathbf{A}\nabla\phi, \tag{1.2}$$

then rewriting the partial differential equation in (1.1) as

$$\nabla \cdot \mathbf{v} = f. \tag{1.3}$$

In the context of reservoir simulation, definition (1.2) is Darcy's law and equation (1.3) is the mass conservation law. In reservoir simulation, this same approach of treating flow velocity explicitly has been used in mixed finite-element methods with considerable success [11],[12],[18].

To continue the derivation of the discretization, assume that \mathbf{A} is a diagonal tensor,

$$\mathbf{A} = \begin{pmatrix} a_x & 0 \\ 0 & a_y \end{pmatrix}.$$

Here, a_x and a_y may be functions of position. Section 3.1, contains the details of the discretization process for the case where \mathbf{A} is a full tensor. Let u and v denote the components of the velocity,

$$(u, v)^t = \mathbf{v}.$$

Then the second-order partial differential equation (1.1) may be written in

the form of a first-order system in Ω :

$$\begin{cases} a_x^{-1}u + \partial\phi/\partial x = 0 & \text{(u equation)} \\ a_y^{-1}v + \partial\phi/\partial y = 0 & \text{(v equation)} \\ \partial u/\partial x + \partial v/\partial y = f & \text{(p equation)}, \end{cases} \quad (1.4)$$

with boundary conditions,

$$\begin{aligned} u(\mathbf{x}) &= g(\mathbf{x}), & \mathbf{x} &\in \partial\Omega_{\text{west}} \cup \partial\Omega_{\text{east}} \\ v(\mathbf{x}) &= g(\mathbf{x}), & \mathbf{x} &\in \partial\Omega_{\text{south}} \cup \partial\Omega_{\text{north}}. \end{aligned}$$

The labels u,v, and p for the three equations in equation (1.4) are introduced simply for convenience.

To discretize this system, we follow the finite volume element (FVE) principles developed in [7],[13],[14]. The two major components of any FVE discretization scheme are the choice of control volumes over which to integrate the continuous equation and the choice of finite element spaces for the unknowns.

First, to introduce the control volumes for the FVE discretization, consider a uniform square mesh Ω^h with mesh size h that covers Ω . We introduce three sets of control volumes, one for each of the three equations in (1.4). Examples of the control volumes are shown in Figure 1.1. We denote by \mathcal{U} the set of all volumes \mathbf{U} that will be used to discretize the u equation in (1.4). Similarly, we use the notation \mathcal{V} and \mathcal{P} for the sets of volumes \mathbf{V} and \mathbf{P} for the v and p equations, respectively. Note that the control volumes \mathbf{P} correspond to the grid blocks defined by Ω^h , the control volumes \mathbf{U} straddle the vertical grid edges of Ω^h , and the control volumes \mathbf{V} straddle the horizontal grid edges of Ω^h .

Figure 1.1: Uniform Grid

Next we will introduce the finite elements for the FVE discretization. For our finite element space, we use the lowest order Raviart-Thomas elements [16],[19] on the the control volumes \mathcal{P} :

$$\begin{aligned} u^h & \text{ is linear in } x \text{ and constant in } y \text{ on each } \mathbf{P} \in \mathcal{P}, \\ v^h & \text{ is linear in } y \text{ and constant in } x \text{ on each } \mathbf{P} \in \mathcal{P}, \\ \phi^h & \text{ is constant on each } \mathbf{P} \in \mathcal{P}. \end{aligned}$$

Note that u^h is continuous across vertical edges of the grid and that v^h is continuous across horizontal edges of the grid. The location of the nodes for each of the unknowns with their indexing is also shown in Figure 1.1. The flux boundary condition in equation (1.1) specifies the values of u^h on the west and east boundaries of Ω and the values of v^h on the north and south boundaries of Ω . Noting some of the characteristics of the finite element spaces, the pressure space contains all functions that are piecewise constant on Ω^h . A typical basis function for u^h is shown in Figure 1.2.

Note that the normal component of this basis function is continuous across all grid edges, is zero on all edges except the edge shared by the two \mathbf{P} volumes which are the support of the function where the normal component equals a nonzero constant. With these properties we can guarantee that the computed flow velocity will also have continuous normal components across grid edges. This will also be the case for general quadrilateral grids as we will see in Section 2.1. The true physical solution also has this property - continuous normal component of velocities - but not every numerical scheme for approximating it does, as [17] pointed out.

Figure 1.2: u Basis Function

We are now ready to discretize the equations. Start by taking the u equation in (1.4) and integrating it over each $\mathbf{U} \in \mathcal{U}$. This will result in a discrete version of Darcy's law. As an example, let $\mathbf{U}_{i,j}$ be the volume in \mathcal{U} that is centered at the interior u^h node (i,j) , as shown in Figure 1.3.

We then have

$$\int_{\mathbf{U}_{i,j}} (a_x^{-1}u + \partial\phi/\partial x) dx dy = 0. \quad (1.5)$$

Consider the two terms in the integral separately. For the first term in equation (1.5), we split the integral into two parts, one for each half of $\mathbf{U}_{i,j}$. This yields,

$$\int_{\mathbf{U}_{i,j}} (a_x^{-1}u) dx dy = \int_{\mathbf{U}_{i,j}^l} (a_x^{-1}u) dx dy + \int_{\mathbf{U}_{i,j}^r} (a_x^{-1}u) dx dy, \quad (1.6)$$

Figure 1.3: $\mathbf{U}_{i,j}$ Volume

where $\mathbf{U}_{i,j}^l$ and $\mathbf{U}_{i,j}^r$ denote the left and right halves of the control volume. Now because the finite element approximation u^h is linear in x and constant in y on each of the halves, by direct calculation it follows that

$$\int_{\mathbf{U}_{i,j}^l} (a_x^{-1} u) dx dy = \frac{h^2}{8} a_x^{-1}(l) (3u_{i,j}^h + u_{i-1,j}^h).$$

A similar expression is obtained for the integral over the right half of $\mathbf{U}_{i,j}$. Note that here we have assumed a_x^{-1} to equal the constant value $a_x^{-1}(l)$ on the left half of the control volume. If it is instead piecewise constant on some finer mesh, as will often be the case in the section on computational results, then the integral can be split into parts on this finer mesh and evaluated. The details of this piecewise integration can be found in Section 3.3, where we show, in the more general case of quadrilateral grids, how to use integrals calculated on fine grids to generate integrals on coarser grids. Now for the second term in equation (1.5), we have

$$\int_{\mathbf{U}_{i,j}} (\partial\phi/\partial x) dx dy = \int_0^h \left(\int_0^h (\partial\phi/\partial x) dx \right) dy.$$

Then apply the divergence theorem to get

$$\int_0^h \left(\int_0^h (\partial\phi/\partial x) dx \right) dy = \int_0^h (\phi(h, y) - \phi(0, y)) dy. \quad (1.7)$$

Then, as the finite element approximation ϕ^h is constant on the vertical edges $x = 0$ and $x = h$, it follows that

$$\int_0^h (\phi(h, y) - \phi(0, y)) dy = h (\phi_{i,j}^h - \phi_{i-1,j}^h). \quad (1.8)$$

Putting these observations together, the discrete equation that equation (1.5) gives rise to is thus

$$\frac{h^2}{8} \left[a_x^{-1}(r) \left(3u_{i,j}^h + u_{i+1,j}^h \right) + a_x^{-1}(l) \left(3u_{i,j}^h + u_{i-1,j}^h \right) \right] + h \left(\phi_{i,j}^h - \phi_{i-1,j}^h \right) = 0.$$

If a_x^{-1} is constant, the equation simplifies to

$$\frac{h^2}{8} a_x^{-1} \left(u_{i-1,j}^h + 6u_{i,j}^h + u_{i+1,j}^h \right) + h \left(\phi_{i,j}^h - \phi_{i-1,j}^h \right) = 0.$$

Note that this expression is quite similar to the expression one would get using standard cell-centered finite differences to approximate Darcy's law:

$$u_{i,j}^h + \frac{a_x}{h} \left(\phi_{i,j}^h - \phi_{i-1,j}^h \right) = 0. \tag{1.9}$$

The difference between the two expressions is that, with the mixed FVE method, tridiagonal mass matrix multiplies the velocities rather than a trivially invertible diagonal matrix. One way of viewing equation (1.9), is as a midpoint rule approximation to the integral in equation (1.6). In Section 1.3, we will show that this can result in less accurate approximations for the velocities. More importantly, as we will see when we consider irregular grids, the mixed FVE method has the property of generating discrete versions of Darcy's law for geometries where it is unclear how to use standard cell-centered finite differences.

Integrating the v equation in (1.4) over an interior \mathbf{V} volume yields a similar discrete expression involving nodal values of v^h and ϕ^h .

To complete the discretization process, integrate the p equation in equation 1.4 over the volume in \mathcal{P} centered at the interior ϕ^h node (i, j) . We denote this volume by $\mathbf{P}_{i,j}$. See Figure 1.4.

Integration is simply a matter of applying the divergence theorem. From the definition of u and v , we have

$$\int_{\mathbf{P}_{i,j}} (\partial u / \partial x + \partial v / \partial y) dx dy = \int_{\mathbf{P}_{i,j}} \nabla \cdot \mathbf{v} dx dy.$$

Transforming the volume integral to a surface integral yields the following:

$$\begin{aligned} \int_{\mathbf{P}_{i,j}} \nabla \cdot \mathbf{v} dx dy &= \int_{\partial \mathbf{P}_{i,j}} \mathbf{v} \cdot \boldsymbol{\eta} ds = \\ &= \int_{\partial \mathbf{P}_{i,j}^e} u dy - \int_{\partial \mathbf{P}_{i,j}^w} u dy + \int_{\partial \mathbf{P}_{i,j}^n} v dx - \int_{\partial \mathbf{P}_{i,j}^s} v dx, \end{aligned}$$

where $\partial \mathbf{P}_{i,j}^e$ denotes the east edge of the control volume, and similarly for the west, north, and south edges. Then, since the finite element approximations u^h and v^h are constant on edges, we have

$$\begin{aligned} &\int_{\partial \mathbf{P}_{i,j}^e} u dy - \int_{\partial \mathbf{P}_{i,j}^w} u dy + \int_{\partial \mathbf{P}_{i,j}^n} v dx - \int_{\partial \mathbf{P}_{i,j}^s} v dx \\ &= h(u_{i+1,j}^h - u_{i,j}^h + v_{i,j+1}^h - v_{i,j}^h). \end{aligned}$$

The discrete version of the p equation in (1.4) is therefore just

$$h(u_{i+1,j}^h - u_{i,j}^h + v_{i,j+1}^h - v_{i,j}^h) = h^2 f_{i,j}.$$

Here, on the right hand side, we have assumed that f is a piecewise constant function on \mathcal{P} , with $f_{i,j}$ denoting the value of f at the ϕ node (i, j) . Another way of looking at this is: we have used the midpoint approximation to the integral; if we had assumed that we had more information about f , we could have used a more accurate approximation for its integral. For example,

Figure 1.4: **P** Volume

knowing f as a function of x and y , we could have used a Gauss quadrature rule to approximate the integral.

In summary, the discretization has produced discrete versions of Darcy's law for each volume $\mathbf{U} \in \mathcal{U}$ and each volume $\mathbf{V} \in \mathcal{V}$. These equations relate the pressure drop between cells to a linear combination of velocities. The discretization has also produced discrete conservation equations for each volume $\mathbf{P} \in \mathcal{P}$. For each \mathbf{P} volume, we have that the discrete flux out of (or into) the volume balances with the strength of the source (or sink) in the volume. This conservative property is an important feature of FVE discretization schemes in general. The mathematical modeling of many physical systems (including flow in porous media) starts with a conservation law stated in integral form. In going from the continuous mathematical model to the discrete mathematical model, preserving some analogy of this conservation law is desirable. For time dependent applications, this discrete conservation property is often necessary to generate acceptable solutions.

The discretization technique described in this section can easily be generalized to handle problems in three dimensions. Also, it can be easily modified to handle the Dirichlet problem, where the flux boundary condition in equation (1.1) is replaced by

$$\phi(\mathbf{x}) = g(\mathbf{x}) \quad \mathbf{x} \in \partial\Omega.$$

In [10] this mixed FVE discretization is applied to Poisson's equation with Dirichlet boundary condition on a three dimensional domain. This reference

contains the details of the necessary modifications.

1.2 An FVE Based Multigrid Algorithm

We begin with a very brief overview of multigrid fundamentals, assuming that the reader is already somewhat familiar with the field. Good references are the introductory ‘tutorial’ [6] and the advanced ‘guide’ [3]. Another useful reference is [14], which presents multigrid (and multilevel adaptive) methods for use in conjunction with FVE discretization techniques.

Consider the problem of finding the solution to the discrete set of equations

$$L^h u^h = f^h. \tag{1.10}$$

We think of equation (1.10) as coming from the discretization of some continuous partial differential equation on a uniform grid with mesh size h , although multigrid methods can be applied to discrete problems with no continuous origin (e.g., [4]). If the number of unknowns is too large to solve the equation directly, one might try simple Gauss-Seidel relaxation to find an approximate solution, \hat{u}^h , to (1.10). One typically finds that the convergence speed of this process degrades very early in the iterations: the first few relaxation sweeps may substantially reduce the residual

$$r^h \equiv f^h - L^h \hat{u}^h,$$

but, subsequent relaxation sweeps do not. The problem is that relaxation methods generally do not reduce low-frequency errors very well. In multigrid

methods, coarser grids are used to solve for and then eliminate this low-frequency error that relaxation alone cannot resolve. This is done by way of the error equation

$$L^h e^h = r^h, \quad (1.11)$$

where e^h denotes the error in the current approximation:

$$e^h = u^h - \hat{u}^h.$$

Because relaxation does work well for high-frequency error, after a few relaxation sweeps one can represent the error accurately on a coarser grid. With this in mind, we consider a coarse grid version of equation (1.11):

$$L^{2h} u^{2h} = I_h^{2h} r^h. \quad (1.12)$$

Here we think of the operator L^{2h} as coming from the discretization of the same continuous partial differential equation on a uniform grid, but with twice the mesh size as the original problem (1.10). The operator I_h^{2h} is called the restriction operator and is used to transfer the fine grid function r^h to the coarser grid. One may be able to solve equation (1.12) exactly for u^{2h} , remembering that this system is on a coarser grid so it is not as large as the original one. Then one would correct the fine grid approximation by u^{2h} , which is approximately equal to the error in \hat{u}^h , according to

$$\hat{u}^h \leftarrow \hat{u}^h + I_{2h}^h u^{2h}. \quad (1.13)$$

Here, the operator I_{2h}^h , called the interpolation operator, is used to transfer the coarse grid function u^{2h} to the fine grid. We now perform a few relaxation

sweeps to reduce any high-frequency error that we may have introduced. This completes one multigrid cycle, the steps of which were:

- 1) Relax the fine grid problem.
- 2) Form the coarse grid version of the error equation.
- 3) Solve the coarse grid version of the error equation.
- 4) Correct the fine grid approximate solution.
- 5) Relax the fine grid problem.

In practice, one may not be able to solve the coarse grid version of the error equation for the same reasons one cannot solve the original problem: it is still too large, so that relaxation alone does not work and direct methods are too expensive. One then can use the above multigrid cycle recursively on this problem, using a still coarser grid with mesh size $4h$. This process can be continued until a coarse enough grid is reached, where a direct method or relaxation by itself is effective. One multigrid cycle is represented graphically in Figure 1.5.

The basic components of a multigrid algorithm are the grids themselves, the discrete operators on each grid ($L^h, L^{2h}, L^{4h}, \dots$), the relaxation process, and the grid transfer operators (interpolation and restriction). The multigrid method is an iterative method, but typically one needs only a few cycles to produce a good approximation. Moreover, the so-called full multigrid algorithms, which start with multigrid cycles applied to coarser levels, can achieve approximations with accuracy comparable to the exact discrete solution in the equivalent of just two or three fine grid cycles.

Now to develop a multigrid algorithm designed specifically for solving

Figure 1.5: One Multigrid Cycle

the discrete set of equations generated by the mixed FVE discretization of the previous section, consider a family of uniform square grids Ω^h of mesh size h that cover the region Ω . Figure 1.6 shows a coarse grid Ω^{2h} , with twice the mesh size of the grid Ω^h in Figure 1.1. Note that the coarse grid ‘looks’ like the fine grid. Simply joining four square fine grid cells produces a square coarse grid cell (for the general quadrilateral grids in Section 2.2 producing coarse grids from fine grids is not so simple). On each grid Ω^h , we can apply the mixed FVE discretization process, and we write the discrete set of equations that this process generates as

$$L^h z^h = g^h, \tag{1.14}$$

where $z^h = (u^h, v^h, \phi^h)^t$ and $g^h = (f_u^h, f_v^h, f^h)^t$, with the unknowns u^h , v^h , and ϕ^h being the nodal values of the corresponding functions u, v , and ϕ on grid Ω^h . Note that, in the FVE discretization of the previous section, f_u^h and f_v^h were zero. In the multigrid algorithm, on coarse grids these will, in general, be non-zero when we form the coarse grid version of the error equation.

We now must define interpolation and restriction operators and a relaxation process. For defining interpolation operators, we use the same general principles as outlined in [14], but we must be specific here. The finite volume element discretization is based on finite element spaces for the variables u^h, v^h , and ϕ^h , so we can simply use the relationship between the finite element spaces of the different grids to define interpolation. In particular, the

Figure 1.6: Uniform Coarse Grid

finite element spaces are nested in that one can write a coarse grid basis function as a linear combination of fine grid basis functions. This nesting property simplifies the definition of interpolation operators. To define the interpolation operator for ϕ , $I(\phi)_{2h}^h$, note that ϕ^{2h} is constant on the grid $2h$ volume $\mathbf{P}_{I,J}$. Referring to Figure 1.7, we thus have the following characterization of $\phi^h = I(\phi)_{2h}^h \phi^{2h}$:

$$\phi_{i,j}^h = \phi_{i+1,j}^h = \phi_{i,j+1}^h = \phi_{i+1,j+1}^h = \phi_{I,J}^{2h}. \quad (1.15)$$

To define the interpolation operator for u , $I(u)_{2h}^h$, note that u^{2h} is linear in x and constant in y on the grid $2h$ volume $\mathbf{P}_{I,J}$. We thus have the following characterization of $u^h = I(u)_{2h}^h u^{2h}$ (see Figure 1.7):

$$\begin{aligned} u_{i,j}^h &= u_{i,j+1}^h = u_{I,J}^{2h}, \\ u_{i+2,j}^h &= u_{i+2,j+1}^h = u_{I+1,J}^{2h}, \\ u_{i+1,j}^h &= u_{i+1,j+1}^h = 1/2(u_{I+1,J}^{2h} + u_{I,J}^{2h}). \end{aligned} \quad (1.16)$$

Definition of the interpolation operator for v is similar.

For defining restriction operators, we again use the same general principles as outlined in [14]. In the multigrid algorithm, restriction operators are used to transfer right hand sides and residuals of equations, not the unknowns themselves. The definitions of the restriction operators are therefore naturally based on the relationship between the volumes of the various grids. The idea is to lump several of the grid h right hand sides to produce the grid $2h$ right hand sides. To define the restriction operator for the P equation, $I(P)_h^{2h}$, note that a grid $2h$ volume $\mathbf{P}_{I,J}$ consists of four of the \mathbf{P} volumes

Figure 1.7: Fine and Coarse Grids, I

of grid h . We thus have the following characterization of $f^{2h} = I(P)_h^{2h} f^h$, referring again to Figure 1.7:

$$f_{I,J}^{2h} = f_{i,j}^h + f_{i+1,j}^h + f_{i,j+1}^h + f_{i+1,j+1}^h. \quad (1.17)$$

To define the restriction operator for the U equation, $I(U)_h^{2h}$, note that a grid $2h$ volume $\mathbf{U}_{I,J}$ of Ω^{2h} contains all of two of the \mathbf{U} volumes of grid h and half of four others. We thus have the following characterization of $f_u^{2h} = I(U)_h^{2h} f_u^h$, referring to Figure 1.8:

$$f_{u\ I,J}^{2h} = f_{u\ i,j}^h + f_{u\ i,j+1}^h + \frac{1}{2}(f_{u\ i-1,j}^h + f_{u\ i-1,j+1}^h + f_{u\ i+1,j}^h + f_{u\ i+1,j+1}^h). \quad (1.18)$$

Definition of the restriction operator for the V equation is done in a similar fashion.

For the equations on grid Ω^h , there are a variety of relaxation techniques one could use. We will present the two that have proved to be most efficient in our numerical experiments: distributive Gauss-Seidel relaxation and box Gauss-Seidel relaxation. We consider these two relaxation schemes because there is no one-to-one correspondence between equations and unknowns (point Gauss-Seidel makes no sense per se). There are three types of discrete equations:

$$\begin{aligned} &\text{U equations:} \\ &\frac{h^2}{8} a_x^{-1} (u_{i-1,j}^h + 6u_{i,j}^h + u_{i+1,j}^h) + h (\phi_{i,j}^h - \phi_{i-1,j}^h) = f_{u\ i,j}^h, \\ &\text{V equations:} \\ &\frac{h^2}{8} a_y^{-1} (v_{i,j-1}^h + 6v_{i,j}^h + v_{i,j+1}^h) + h (\phi_{i,j}^h - \phi_{i,j-1}^h) = f_{v\ i,j}^h, \\ &\text{P equations:} \\ &h(u_{i+1,j}^h - u_{i,j}^h + v_{i,j+1}^h - v_{i,j}^h) = h^2 f_{i,j}. \end{aligned} \quad (1.19)$$

Figure 1.8: Fine and Coarse Grids, II

Again, we point out that the labels are used only for convenience; for example, there is no inherent reason to associate the P equation closely with the ϕ variable and, in fact, it does not even appear in this equation.

The ‘guide’ [3] contains an excellent description of distributive Gauss-Seidel relaxation schemes, so that here we will be content with a brief description of our scheme. We can naturally associate the U equations with the velocity variable $\mathbf{u}_{i,j}^h$ of the grid edge that the \mathbf{U} volume straddles. Likewise, we can naturally associate the V equations with the velocity variable $\mathbf{v}_{i,j}^h$ of the grid edge that the \mathbf{V} volume straddles. We therefore relax these equations using standard point Gauss-Seidel relaxation. The basic idea is to relax the U, V, and P equations together locally in such a way that the error is smoothed while the U and V equations are not “damaged”, i.e., their residuals are essentially unchanged. We can think of the overall relaxation process (including point Gauss-Seidel for U and V) as a three step scheme. First, we sweep over all of the u^h nodes, change the value of $u_{i,j}^h$ in turn so that the U equation at (i, j) is satisfied. Second, we perform a similar Gauss-Seidel relaxation of all of the V equations. Note that these two steps, U and V relaxation, are independent of each other and could be performed in parallel. In fact, for full independence, point Jacobi could be used within each variable without much loss of efficient smoothing because of the associated tridiagonal mass matrix. Finally, we sweep over each ϕ^h node in turn, simultaneously changing the value of $\phi_{i,j}^h$ and the values of u^h and v^h that

lie on the edge of the volume $\mathbf{P}_{i,j}$ (namely, $u_{i,j}^h$, $u_{i+1,j}^h$, $v_{i,j}^h$, and $v_{i,j+1}^h$) so that the \mathbf{P} equation at (i,j) is satisfied and so that the residuals of the \mathbf{U} equations at (i,j) and $(i+1,j)$ and of the \mathbf{V} equations at (i,j) and $(i,j+1)$ are unchanged. To allow for effective vectorization, the Gauss-Seidel relaxation process in each of these three steps is done using a red/black ordering.

The second technique we consider is box relaxation. This approach involves only one step, which consists of a sweep over each \mathbf{P} volumes in turn changing the values of the associated five unknowns $\phi_{i,j}^h$, $u_{i,j}^h$, $u_{i+1,j}^h$, $v_{i,j}^h$, and $v_{i,j+1}^h$ so that the corresponding five equations are satisfied. We will often need to use a y-line box Gauss-Seidel relaxation technique, which is the same as box relaxation except that all of the \mathbf{P} volumes sharing the same i index are relaxed simultaneously as a group. Analogously, x-line box Gauss-Seidel involves relaxing all \mathbf{P} volumes that share the same j index as a group. We will use the term xy or alternating line relaxation to signify a single relaxation step where we perform x-line relaxation followed by y-line relaxation. As will be evident from the results of numerical experiments the best choice of relaxation technique, in the sense of the most efficient solver, is problem dependent. The line relaxation techniques are clearly computationally more expensive; but for problems with anisotropic coefficients, line relaxation is often needed to achieve acceptable convergence rates for the multigrid algorithm.

1.3 Computational Results

The major motivation in developing the mixed FVE discretization approach was to have an accurate discretization for irregular grids, where there is no clear way to use standard cell-centered finite differences. However, a case can be made for using the mixed FVE discretization even on uniform grids, as we will demonstrate in this section.

1.3.1 Comparison to Finite Differences for Poisson Problem

We begin with the simplest of problems of the type to which our discretization applies, namely Poisson's equation on the square domain $\Omega = [-1, 1]^2$:

$$\begin{cases} -\nabla \cdot \nabla \phi(\mathbf{x}) = f(\mathbf{x}) & \mathbf{x} \in \Omega, \\ \nabla \phi(\mathbf{x}) \cdot \eta = g(\mathbf{x}) & \mathbf{x} \in \partial\Omega \end{cases} \quad (1.20)$$

One can write this equation as a system of first-order equations in the way presented in Section 1.1, then apply the mixed FVE discretization. We will call this the mixed FVE approach. Alternatively, one could discretize equation (1.20) using standard cell-centered finite differences, then solve the resulting discrete set of equations for an approximation to ϕ . If we were interested in approximations to velocities or fluxes, we could then apply appropriate standard finite differencing to the approximation of ϕ . We will call this the finite difference approach.

To compare these two approaches, consider the function

$$\phi(x, y) = \cos(k_1 \pi x) + \cos(k_2 \pi y), \quad (1.21)$$

where k_1 and k_2 are integers. If we set

$$\begin{aligned} f(x, y) &= \pi^2(k_1^2 + k_2^2)(\cos(k_1\pi x) + \cos(k_2\pi y)), \\ g(x, y) &= 0 \end{aligned}$$

in equation (1.20), then the function in (1.21) is a solution to the partial differential equation. It is not the only solution because we can add an arbitrary constant to the solution ϕ , while preserving the property of satisfying the partial differential equation and boundary condition. The function in (1.21) is the unique solution that satisfies the additional condition that its integral over Ω is zero. By varying k_1 and k_2 , one can see the effect that oscillations in the true solution have on the accuracy of the numerical solutions generated by a mixed FVE approach and a finite difference approach. We measure the error in the solutions in the following way. For the mixed FVE approach, we calculate the \mathcal{L}^2 norm of $\phi - \phi^{m, fve}$ and call this quantity $\phi_e^{m, fve}$. Because the mixed FVE discretization relies on finite element spaces, one has an approximation to ϕ everywhere in Ω except at grid interfaces, so the \mathcal{L}^2 norm make sense. For the straightforward finite difference approach, one has approximation to ϕ only at the nodes. To create a functional approximation to ϕ , we assume that the nodal approximation holds for the entire cell, then calculate the \mathcal{L}^2 norm of its difference with the exact solution. We call this quantity $\phi_e^{f, d}$. Because we are interested in accurate approximation of velocities, which are here just the components of the gradient of ϕ , we measure the error in them as well, which we do in the following way. For the

mixed FVE approach, we calculate the difference between the fluxes,

$$\int_{\epsilon} \mathbf{v} \cdot \boldsymbol{\eta} ds$$

using the exact and the approximate solutions over each grid edge. We then take the ℓ^2 norm of the difference on vertical edges and call this u_e^{mfve} . Analogously, we take the ℓ^2 norm of the difference on horizontal edges and call this v_e^{mfve} . Note that if the exact velocity is \mathbf{V} and the mixed FVE approximation is \mathbf{v} , then $((u_e^{mfve})^2 + (v_e^{mfve})^2)^{\frac{1}{2}}$ is equivalent to a discrete $H(\text{div})$ norm of the vector velocity error (which incorporates \mathcal{L}^2 norms of $(\mathbf{v} - \mathbf{V})_x$, $(\mathbf{v} - \mathbf{V})_y$, and $\text{div}(\mathbf{v} - \mathbf{V})$, the last of which is zero by the local conservation property of the mixed FVE method). For the finite difference approach, we do the same to calculate u_e^{fd} and v_e^{fd} . To get approximations for ϕ , we use standard finite differencing of the approximation of ϕ .

Tests were run on a grid with 64 cells in each direction and the results are shown below.

Mixed FVE				
k_1	k_2	ϕ_e^{mfve}	u_e^{mfve}	v_e^{mfve}
1	1	4.01E-2	2.52E-6	2.52E-6
1	4	1.17E-1	1.74E-2	4.38E-3
1	8	2.27E-1	7.14E-2	9.16E-3
1	12	3.37E-1	1.44E-1	1.28E-2
1	16	4.41E-1	2.10E-1	1.49E-2
15	13	5.27E-1	2.59E-1	2.92E-1

Finite Difference				
k_1	k_2	ϕ_e^{fd}	u_e^{fd}	v_e^{fd}
1	1	4.01E-2	3.89E-12	3.89E-12
1	4	1.17E-1	3.56E-2	8.96E-3
1	8	2.32E-1	1.57E-1	2.02E-2
1	12	3.53E-1	3.62E-1	3.20E-2
1	16	4.84E-1	6.55E-1	4.51E-2
15	13	5.46E-1	8.79E-1	9.92E-1

One can see that both methods produce approximations to ϕ of roughly equal quality. When the solution is smooth, the approximations to the fluxes are also of equal quality. However, for oscillatory solutions, i.e., increasing k_2 ($k_2 = 16$ is the most oscillatory function that can be represented on this grid), the mixed FVE obtains somewhat more accurate approximations to the fluxes. This is also true for the last case where the solution oscillates in both directions. This is not surprising considering that one can view the finite difference approach as a midpoint rule approximation of the integral in the Darcy equation, as mentioned in Section 1.1. This approximation is accurate for smooth functions, but not so accurate for more oscillatory ones.

To be fair in comparing these two approaches, one should also consider the work necessary to generate the approximations. For solving the equations in the finite difference approach, we used black box multigrid [8]. This code is aimed at solving much more difficult problems than Poisson's equation, as we will say more about later, and is therefore not the most efficient code for such a simple problem. For solving the mixed FVE equations, we used the multigrid algorithm of the previous section with distributive relaxation. Both

multigrid methods proved to have similar worst-case convergence factors, approximately .1, so that the amount of work for solving the mixed FVE equations would be about three times that for the finite difference equations. Loosely speaking, the factor of three comes from the fact that, in the mixed FVE approach, one has roughly three times the number of equations as in the finite difference approach. A careful comparison of relative costs of the two algorithms should compare relaxation complexity: while the mixed FVE scheme is more involved, its individual stencils are a little smaller, so that the factor of three is still approximately correct. If one were to compare fully optimized codes, we are confident in our belief that the mixed FVE solver would be no worse than three times slower than the finite difference solver. For oscillatory solutions we have seen that the error in the mixed FVE fluxes can be up to three times smaller than the error for the finite difference approach. So one might argue that the comparison comes out very roughly even. However, these tests certainly show that the mixed FVE approach has the potential to generate more accurate approximations for fluxes than the standard finite difference approach even for simple problems, and for slightly more complex problems, the difference in accuracy between the two methods can be much greater as will be shown in the next section.

1.3.2 Discontinuous and Anisotropic Diffusion Coefficients

The results for Poisson's equation, while encouraging, are not of particular interest from the reservoir simulation point of view. In reservoir simulation, the diffusion coefficient \mathbf{A} is typically anisotropic and may have large jumps from grid cell to grid cell. We will now consider these types of problems.

It has been known for some time that to get acceptable multigrid convergence factors for anisotropic problems, one needs a relaxation scheme more complicated than simple point (or cell) relaxation. The reason is that simple point Gauss-Seidel relaxation will smooth the error only between strongly coupled points. For example, consider the diffusion equation

$$-\nabla \cdot \mathbf{A} \nabla \phi(\mathbf{x}) = f(\mathbf{x}), \quad \mathbf{x} \in \Omega,$$

where

$$\mathbf{A} = \begin{pmatrix} 1 & 0 \\ 0 & \epsilon \end{pmatrix}.$$

Standard finite differences and a standard multigrid algorithm with point Gauss-Seidel relaxation leads to extremely poor convergence factors when $\epsilon \ll 1$. In this case, points are much more strongly coupled with neighboring points in the x direction than in the y direction. Local mode analysis [3] shows that point Gauss-Seidel relaxation will only smooth the error effectively in the x direction. Therefore, one cannot properly represent the error on a grid that is coarser in the y direction. One alternative is to accept

this smoothing limitation and only coarsen in the x direction, an approach that has been used in reservoir simulation in [9]. Another alternative is to relax as a group all of the points that are strongly coupled, which, in this case, consists of those points that share the same y coordinate. This x -line relaxation will smooth the error in the weakly coupled direction (the y direction). Then one can represent the error well on a grid that is coarser in the y direction. The distributive relaxation scheme as previously discussed is a single cell relaxation scheme. Only unknowns associated with a particular cell are updated together, and we cannot hope to get acceptable multigrid convergence rates with it for anisotropic problems. The alternative we choose is line relaxation as discussed in Section 1.2. It may often be the case that the strong coupling is in the x direction in parts of the domain and in the y direction in other parts. For these problems, we will need to use alternating line relaxation. An alternative, that we will not consider in this thesis, would be to use semi-coarsening in one of the directions and line relaxation in the other as in [9].

Later we will discuss in more detail problems with the multigrid algorithm when the diffusion coefficient jumps from cell to cell. However, the algorithm as presented in the previous section yields quite acceptable convergence rates when the jumps in the diffusion coefficient occur (if at all) at grid interfaces on the coarsest grid.

We will now present a single numerical example that illustrates the abil-

ity of the multigrid solver to deal with both anisotropic and discontinuous diffusion coefficients. Consider

$$\begin{cases} a_x^{-1}u + \partial\phi/\partial x = 0 \\ a_y^{-1}v + \partial\phi/\partial y = 0 \\ \partial u/\partial x + \partial v/\partial y = f \end{cases}$$

with boundary conditions

$$\begin{aligned} u(\mathbf{x}) &= g(\mathbf{x}), & \mathbf{x} &\in \partial\Omega_{\text{west}} \cup \partial\Omega_{\text{east}} \\ v(\mathbf{x}) &= g(\mathbf{x}), & \mathbf{x} &\in \partial\Omega_{\text{south}} \cup \partial\Omega_{\text{north}}. \end{aligned}$$

The domain of the problem, along with values of a_x and a_y , is shown in Figure 1.9. Note that this problem has regions of strong coupling in the x direction and regions of strong coupling in the y direction. The diffusion coefficient also has lines of discontinuity, although they correspond to grid edges on the coarsest (2 by 2) grid. To obtain asymptotic estimates, the right hand side f and the boundary condition g were set to zero, a random initial guess was used, and ten or more multigrid cycles were performed. We then calculated the geometrically averaged convergence factor (factor by which the residuals are reduced per cycle). The results are shown below.

Grid Size	Convergence Factor
8 × 8	.04
16 × 16	.10
32 × 32	.18
64 × 64	.20

Alternating line relaxation was used with two pre-relaxations and one post-relaxation. We see acceptable convergence factors in that they are fairly small and seem to stabilize as the number of unknowns is increased.

Figure 1.9: Problem Domain

Comparing the mixed FVE method to standard cell-centered finite differences, the greater accuracy of the mixed FVE method is much more evident when the diffusion coefficient is discontinuous. Below we present results for a problem where \mathbf{A} is a scalar, but discontinuous. The domain Ω is $[-1, 1]^2$ and the diffusion coefficient has the following values:

$$\begin{aligned} 0.05 & \text{ for } x > 0, y > 0 \\ 0.01 & \text{ for } x < 0, y > 0 \\ 10.0 & \text{ for } x < 0, y < 0 \\ 33.33 & \text{ for } x > 0, y < 0. \end{aligned}$$

Boundary conditions specified the normal component of velocity to be 1 on the left and right edges of the domain and 0 (no flow) on the top and bottom. Because an analytic solution for the problem was not available, the mixed FVE solution from a 256×256 grid was used as the “exact” solution in calculating errors. The velocity errors, measured in the same way as in the last section, for the mixed FVE solution and the finite difference solution are shown below. The finite difference discretization used harmonic averaging of the diffusion coefficient at interfaces as is standard.

Mixed FVE		
Grid Size	u_e^{mfve}	v_e^{mfve}
2×2	3.26E-1	9.53E-1
4×4	2.25E-2	2.86E-2
8×8	1.04E-2	1.94E-2
16×16	5.01E-3	1.03E-2
32×32	2.46E-3	5.19E-3
64×64	1.18E-3	2.49E-3
128×128	4.89E-4	1.00E-3
256×256	0	0

Finite Differences		
Grid Size	u_e^{fd}	v_e^{fd}
2×2	8.28E-1	9.53E-1
4×4	4.77E-1	5.03E-1
8×8	2.70E-1	3.07E-1
16×16	1.47E-1	1.69E-1
32×32	7.94E-2	9.02E-2
64×64	4.23E-2	4.77E-2
128×128	2.24E-2	2.51E-2
256×256	1.18E-2	1.35E-2

The superiority of the mixed FVE approach is clear; it computes more accurate velocities on a 16×16 grid than finite differences does on a 256×256 grid. This is not an artifact of using the 256×256 mixed solution as “exact,” since the 128×128 and 256×256 finite difference solutions differ from each other by an order of magnitude more than the corresponding mixed solutions differ from each other. As in the comparison of the previous section, the two methods exhibit comparable accuracy for the pressure (not shown). When comparing solutions on different size grids, the mixed velocities do not show second-order convergence as they will in all other tests reported in this thesis. The reason being that the true solution has a singularity at the origin, and thus we cannot expect second-order convergence.

1.3.3 An Alternative Multilevel Algorithm

A Two-Level Approach

We pointed out in the last section that the multigrid algorithm presented in Section 1.2 is robust with respect to jumps in the diffusion coefficient as

long as those jumps occur (if at all) at grid edges on the coarsest grid. For a given diffusion coefficient, this limits the number of levels one can use in the multigrid algorithm: we can coarsen the grid only to the level of the jumps in the diffusion coefficient. If the diffusion coefficient has only a few lines of discontinuity, this is acceptable. However, if the diffusion coefficient has many lines of discontinuity, the coarsest grid we can use may be too fine; there may be too many unknowns to solve the coarse grid version of the error equation well enough, and we must clearly seek an alternative.

The problem that the previous multigrid algorithm has with jumps in the diffusion coefficient that do not occur at interfaces of the coarsest grid can be traced to interpolation. The piecewise constant interpolation scheme defined in (1.15) is suitable so long as the diffusion coefficient is continuous within the coarse grid cell. To illustrate the problem that arises when this is not the case, consider the extreme situation shown in Figure 1.10.

In the two fine grid cells on the right, there is no flow and $\phi = 0$; these are ‘dead’ cells. In the two fine grid cells on the left, ϕ is non-zero; these are ‘live’ cells. If we use piecewise constant interpolation from the coarse grid cell, which will generally be ‘live’, then we can expect to interpolate some nonzero value of ϕ to the two ‘dead’ cells, which is completely incorrect. The solution to this problem, as discussed in [1], is to use information about the diffusion coefficient in interpolating ϕ . This is the basis of the algorithm for black box multigrid [8], a robust multigrid solver for the diffusion equation

Figure 1.10: 'Live' and 'Dead' Cells

with strongly discontinuous coefficients. It may be possible to incorporate this operator-based interpolation into the previous multigrid algorithm, but we choose instead a different more convenient approach.

We will explain the approach as a two-level multigrid algorithm, although this is somewhat of a misnomer since we will have only one grid. Consider the fine level problem as the mixed FVE discretization of the first-order system

$$\begin{aligned} \mathbf{A}^{-1}\mathbf{v} + \nabla\phi &= 0, \\ \nabla \cdot \mathbf{v} &= f. \end{aligned}$$

We write the mixed FVE equations in matrix form as

$$\begin{pmatrix} M & grad_h \\ div_h & 0 \end{pmatrix} \begin{pmatrix} \mathbf{v}_h \\ \phi_h \end{pmatrix} = \begin{pmatrix} 0 \\ f_h \end{pmatrix}. \quad (1.22)$$

Here, M is the mass matrix that comes from the integration of Darcy's equation and $grad_h$ and div_h are the grid h discrete operators corresponding to the continuous operators $grad$ and div . Define the residuals according to,

$$\begin{pmatrix} r_{\mathbf{v}}^h \\ r_{\phi}^h \end{pmatrix} = \begin{pmatrix} 0 \\ f_h \end{pmatrix} - \begin{pmatrix} M & grad_h \\ div_h & 0 \end{pmatrix} \begin{pmatrix} \hat{\mathbf{v}}_h \\ \hat{\phi}_h \end{pmatrix}, \quad (1.23)$$

where the variables with hats denote a current approximate solution to equation (1.22). Define the errors by

$$\begin{aligned} e_{\mathbf{v}}^h &= \mathbf{v}^h - \hat{\mathbf{v}}^h, \\ e_{\phi}^h &= \phi^h - \hat{\phi}^h. \end{aligned}$$

The error equation is then,

$$\begin{pmatrix} M & grad_h \\ div_h & 0 \end{pmatrix} \begin{pmatrix} e_{\mathbf{v}}^h \\ e_{\phi}^h \end{pmatrix} = \begin{pmatrix} r_{\mathbf{v}}^h \\ r_{\phi}^h \end{pmatrix}. \quad (1.24)$$

Now, rather than using a coarser grid with the mixed FVE discretization to approximate the error equation, use the same grid with a standard cell-centered finite difference approximation. This is the ‘coarse’ level in our multigrid algorithm. The ‘coarse’ grid version of the error equation can then be written in matrix form as

$$\begin{pmatrix} \tilde{M} & grad_h \\ div_h & 0 \end{pmatrix} \begin{pmatrix} \mathbf{v}^h \\ \phi^h \end{pmatrix} = \begin{pmatrix} r_{\mathbf{v}}^h \\ r_{\phi}^h \end{pmatrix}. \quad (1.25)$$

The only difference between equations (1.24) and (1.25) is the mass matrix. In (1.25) the mass matrix \tilde{M} is diagonal and computed from the diffusion coefficient using harmonic averaging at discontinuities. The point is that, in equation (1.25), we can eliminate the velocity variables. We have

$$\mathbf{v}^h = \tilde{M}^{-1} (grad_h \phi_h + r_{\mathbf{v}}^h). \quad (1.26)$$

This allows us to rewrite equation (1.25) as

$$-div_h \tilde{M}^{-1} grad_h \phi_h = r_{\phi}^h - div_h \tilde{M}^{-1} r_{\mathbf{v}}^h. \quad (1.27)$$

This is just the type of equation for which black box multigrid was developed. Our approach is then to use black box multigrid to solve this equation for ϕ , use equation (1.26) to get \mathbf{v}^h , and these approximations of the error to correct our mixed FVE approximation.

This two-level approach is similar to the work in [15], where black box multigrid was used as a ‘coarse’ level for a Lagrangian hydrodynamics application. In different vein, this two-level approach is similar to preconditioning

the mass matrix M by its diagonal. This approach was suggested, in the context of mixed finite element methods in [18].

Two-Level Computational Results

We present here the results from a single numerical experiment to test the robustness of the two-level approach with respect to discontinuities in the diffusion coefficient. The diffusion coefficients a_x and a_y were separately and randomly assigned a value between .01 and 100 for each grid cell. The diffusion coefficient is thus anisotropic and has jumps of several orders of magnitude between cells. The two-level algorithm described in the previous section was used, with two alternating line relaxation sweeps on the mixed FVE equations before using black box multigrid to solve the ‘coarse’ problem and one alternating line relaxation sweep after. One point to consider is: how well do we need black box multigrid to solve the ‘coarse’ problem? In [15] only one cycle of black box multigrid was used for this purpose. For this difficult test problem (note: black box multigrid convergence factors were approximately .6), we found that performing more than one cycle of black box multigrid improved the overall convergence of the two-level method. In the results reported below, five cycles of black box multigrid are used to approximate the ‘coarse’ problem solution, although fewer, say 2 or 3, are often enough to obtain similar two-level convergence factors. The asymptotic convergence factors for the two-level method are given below.

Grid Size	Convergence Factor
16×16	.43
32×32	.44
64×64	.46

We see that, although the factors are much less impressive than they are for Poisson type applications, especially when work is considered, this two-level approach does exhibit convergence factors that seem to be bounded with growing problem size. One point about these relatively “poor” convergence factors (for comparison, the convergence factors of this two-level algorithm for constant coefficient problems is .1), these results show that, for this problem, there is a significant difference between the mixed FVE discretization and the standard finite-difference approach. This difference was illustrated in the numerical tests of Section 1.3.2. When these two approaches are “close”, the diagonal mass matrix \tilde{M} is an excellent approximation to the mixed FVE mass matrix M , and the two-level method converges quickly. Alternatively, when the two-level method converges relatively slowly, the two approaches are significantly different, and we have seen that the mixed FVE approach can be much more accurate.

The point of considering this two-level method was to allow treatment of problems where the coarsest grid for the multigrid algorithm presented in Section 1.2 is still too fine and has too many unknowns to solve the mixed FVE equations by itself. In practice, the multigrid algorithm presented in Section 1.2 could be used down to the coarsest grid that was aligned with the discontinuities in the diffusion coefficient, where the two-level approach

described here could be applied.

1.3.4 Full Tensor Diffusion Coefficients

In this section we present results of two calculations with full tensor diffusion coefficients on uniform grids. The derivation of the mixed FVE Darcy equation for this case is discussed in Section 3.1.

In the first problem, the diffusion coefficient \mathbf{A} is constant throughout the domain $\Omega = [-1, 1]^2$ and given by

$$\mathbf{A} = \begin{pmatrix} \cos \theta & \sin \theta \\ -\sin \theta & \cos \theta \end{pmatrix} \begin{pmatrix} 1 & 0 \\ 0 & 0.01 \end{pmatrix} \begin{pmatrix} \cos \theta & -\sin \theta \\ \sin \theta & \cos \theta \end{pmatrix},$$

where θ is the angle between the coordinate axes and the principal directions of permeability. The boundary conditions and source term f were set so that the exact solution to the problem (with integral over $\Omega = 0$) is

$$\phi(x, y) = \cos(\pi x) \cos(2\pi y).$$

The mixed FVE discretization was solved on uniform grids of various sizes and for various values of the angle θ . The errors in the resulting approximations are shown below (measured in the same way as in previous sections).

$\theta = 0^\circ$			
Grid Size	ϕ_e^{mfve}	u_e^{mfve}	v_e^{mfve}
8×8	0.4804	5.942E-3	3.216E-3
16×16	0.2501	2.140E-3	1.091E-3
32×32	0.1263	5.708E-4	2.868E-4
64×64	0.0633	1.449E-4	7.252E-5

$\theta = 15^\circ$			
Grid Size	ϕ_e^{mfve}	u_e^{mfve}	v_e^{mfve}
8×8	1.836	1.925E-1	8.872E-2
16×16	0.5551	6.959E-2	3.024E-2
32×32	0.1803	1.949E-2	8.268E-3
64×64	0.0712	5.035E-3	2.119E-3

$\theta = 30^\circ$			
Grid Size	ϕ_e^{mfve}	u_e^{mfve}	v_e^{mfve}
8×8	4.684	1.084E-1	6.844E-2
16×16	1.250	4.353E-2	2.733E-2
32×32	0.3357	1.391E-2	8.679E-3
64×64	0.1006	3.805E-3	2.368E-3

$\theta = 45^\circ$			
Grid Size	ϕ_e^{mfve}	u_e^{mfve}	v_e^{mfve}
8×8	6.575	4.624E-1	3.577E-1
16×16	1.912	1.987E-1	1.568E-1
32×32	0.5254	6.324E-2	5.076E-2
64×64	0.1453	1.715E-2	1.385E-2

From the results we see, not surprisingly, that the accuracy of the discretization degrades as the angle θ grows. However, the results show second order convergence in the velocities even when the anisotropy is not aligned with the grid, so that any practical accuracy could likely be obtained by refining the grid. When the anisotropy is not aligned with the grid, say, $\theta = 45^\circ$, the convergence factors for the mixed FVE multigrid algorithm degrade (average convergence factors of about .5 using alternating line relaxation), just as the discretization accuracy does. Because the strongly coupled points are at a 45° angle, convergence factors of .1 could likely be recovered by block relaxation in this direction. However, this specialized treatment (block relax-

ation in the dominant direction) would be difficult to implement in practice, where the dominant direction would vary throughout the domain.

The second problem is similar to the test problem in [2]. Here the grid is uniform, and \mathbf{A} is a full tensor but no longer constant throughout the domain $\Omega = [0, 1]^2$. The value of the diffusion coefficient is given by

$$\begin{aligned}
 & 0 < x < .5 & .5 < x < 1 \\
 & \mathbf{A} = \begin{pmatrix} \frac{14}{9} & \frac{7}{9} \\ \frac{7}{9} & 2 \end{pmatrix} & \mathbf{A} = \begin{pmatrix} 1 & \frac{1}{2} \\ \frac{1}{2} & 2 \end{pmatrix}.
 \end{aligned}$$

The boundary conditions and source term f were set so that the exact solution is

$$\begin{aligned}
 & 0 < x < .5 & .5 < x < 1 \\
 & \phi = 1 - x^3 + C & \phi = \frac{7}{6}(1 - x^2) + C,
 \end{aligned}$$

where the value of C was chosen to make the integral of ϕ over Ω vanish. Below are the mixed FVE discretization errors, measured in the same way as before, for various grid sizes.

Grid Size	ϕ_e^{mfve}	u_e^{mfve}	v_e^{mfve}
4×4	9.212E-2	4.555E-3	5.748E-3
8×8	4.622E-2	1.110E-3	1.540E-3
16×16	2.313E-2	2.741E-4	3.931E-4
32×32	1.157E-2	6.825E-5	9.871E-5
64×64	5.784E-2	1.755E-5	2.435E-5

In this problem, we clearly see first-order convergence of the pressure and second-order convergence of the velocities. For all test problems with analytic solutions, we have observed second-order convergence of the velocities, and,

as will be shown in the next chapter, the mixed FVE discretization can be extended to general quadrilaterals and still retain this desirable property.

2 General Quadrilateral Grids

2.1 The Mixed FVE Discretization

The focus now is extending the discretization technique of Section 1.1 to irregular grids. We will develop the mixed FVE discretization for a logically rectangular grid of irregular quadrilaterals, an example of which is shown in Figure 2.1. Again, we consider the following partial differential equation defined on some domain Ω , now not necessarily rectangular, in \mathcal{R}^2 :

$$\begin{cases} -\nabla \cdot \mathbf{A} \nabla \phi(\mathbf{x}) & = f(\mathbf{x}) & \mathbf{x} \in \Omega, \\ \nabla \mathbf{A}(\mathbf{x}) \phi(\mathbf{x}) \cdot \eta, & = 0 & \mathbf{x} \in \partial\Omega. \end{cases} \quad (2.1)$$

The diffusion coefficient \mathbf{A} may be a function of position and is not necessarily diagonal; however, it is assumed to be a pointwise symmetric, positive definite matrix.

Again we separate out Darcy's law,

$$\mathbf{A}^{-1} \mathbf{v}(\mathbf{x}) + \nabla \phi(\mathbf{x}) = 0, \quad (2.2)$$

from the conservation of mass equation,

$$\nabla \cdot \mathbf{v}(\mathbf{x}) = f(\mathbf{x}). \quad (2.3)$$

Figure 2.1: General Quadrilateral Grid

We will formulate a mixed FVE discretization for this system of equations that generalizes the mixed FVE discretization presented in Section 1.1.

Important in developing the discretization for general quadrilaterals is the mapping relating a general to a reference quadrilateral. Consider the general quadrilateral P with vertices (x_{00}, y_{00}) , (x_{10}, y_{10}) , (x_{01}, y_{01}) , and (x_{11}, y_{11}) , as shown in Figure 2.2.

Let the reference quadrilateral \hat{P} be the unit square. Then there is a unique bilinear reference mapping of \hat{P} onto P given by

$$\begin{aligned} x(\hat{x}, \hat{y}) &= x_{00} + (x_{10} - x_{00})\hat{x} + (x_{01} - x_{00})\hat{y} + (x_{11} - x_{10} - x_{01} + x_{00})\hat{x}\hat{y}, \\ y(\hat{x}, \hat{y}) &= y_{00} + (y_{10} - y_{00})\hat{x} + (y_{01} - y_{00})\hat{y} + (y_{11} - y_{10} - y_{01} + y_{00})\hat{x}\hat{y}. \end{aligned}$$

If P is convex, then this mapping has an inverse. Since we restrict ourselves to convex quadrilaterals, for each $(x, y) \in P$ we have an associated point $(\hat{x}, \hat{y}) \in \hat{P}$ given by the inverse reference map.

Shown in Figure 2.2 are several vectors that will be useful later in describing the components of our discretization technique: for each $(x, y) \in P$, we define the four vectors

$$\begin{aligned} \mathbf{X}(x, y) &\text{ is the image of the unit vector } (1, 0) \text{ in } \hat{P}, \\ \mathbf{Y}(x, y) &\text{ is the image of the unit vector } (0, 1) \text{ in } \hat{P}, \\ \eta_x(x, y) &\text{ is a unit vector orthogonal to } \mathbf{Y}(x, y), \\ \eta_y(x, y) &\text{ is a unit vector orthogonal to } \mathbf{X}(x, y). \end{aligned}$$

To extend the discretization of Section 1.1 to general quadrilaterals, we need use analogs of the control volumes and finite element spaces used there. For the latter, we use the lowest order Raviart-Thomas elements on the quadrilateral elements (see [5],[19]), which are defined as follows. The char-

Figure 2.2: General Quadrilateral

acteristic functions of the quadrilaterals provide a basis for the finite element space for ϕ . The basis functions for \mathbf{v} are best described in terms of associating degrees of freedom with normal components on edges of quadrilaterals. A typical basis function for the finite element space for \mathbf{v} has support on two adjacent quadrilaterals, a constant normal component on the edge shared by the quadrilaterals, and a normal component of zero on other edges. The magnitude of the basis function is such that the flux on the common edge is one:

$$\int_{edge} \mathbf{v} \cdot \boldsymbol{\eta} ds = 1.$$

These conditions alone do not uniquely determine the basis function; the following additional condition on the finite element space is needed. Within any quadrilateral P , we assume that

$$\begin{aligned} \mathbf{v} \cdot \eta_x \|\mathbf{Y}\| & \text{ varies linearly with } \hat{x}, \text{ constant with } \hat{y}, \\ \mathbf{v} \cdot \eta_y \|\mathbf{X}\| & \text{ varies linearly with } \hat{y}, \text{ constant with } \hat{x}. \end{aligned}$$

A typical basis function is represented in Figure 2.3.

We note that, just as in the uniform grid case, the basis functions have continuous normal components across grid interfaces. So also will our computed solution. The nodes for the unknowns are shown in Figure 2.1. On each grid cell, which we denote by $\mathbf{P}_{i,j}$, we let $\phi_{i,j}^h$ denote the value of the pressure on the cell, and $u_{i,j}^h$, $u_{i+1,j}^h$, $v_{i,j}^h$, and $v_{i,j+1}^h$ the values of the flux on their respective edges. This is a slight departure from the method in Section 1.1 where the unknowns u^h and v^h were defined to be the velocities: applying the method of this section to a uniform grid results in the same

Figure 2.3: Basis Function

equations as in Section 1.1 except for a scaling of the u^h and v^h unknowns by h .

We now need to choose the control volumes. By analogy to the uniform grid case, the quadrilaterals used to describe the grid are the natural choice for the control volumes for equation (2.3). This has the benefit that it leads to a scheme with a local conservation property on these quadrilateral grid cells. To proceed, we integrate equation (2.3), over each grid cell $\mathbf{P}_{i,j}$:

$$\int_{\mathbf{P}_{i,j}} \nabla \cdot \mathbf{v} dx dy = \int_{\mathbf{P}_{i,j}} f.$$

Applying the divergence theorem, we get

$$\int_{\partial \mathbf{P}_{i,j}} \mathbf{v} \cdot \boldsymbol{\eta} ds = \int_{\mathbf{P}_{i,j}} f.$$

The left-hand side of this equation is just the sum of the fluxes on edges of $\mathbf{P}_{i,j}$, so the discretization of the mass conservation equation is

$$u_{i+1,j}^h - u_{i,j}^h + v_{i,j+1}^h - v_{i,j}^h = \int_{\mathbf{P}_{i,j}} f.$$

If we assume that the function f is (approximately) piecewise constant, then we can replace the integral on the right hand side by:

$$f_{i,j} \times AREA(\mathbf{P}_{i,j}).$$

(With more information about f , we could use a more accurate approximation of the integral.)

The control volumes for Darcy's equation generalize the control volumes we used for the uniform grid case. Consider two adjacent grid cells, $\mathbf{P}_{i-1,j}$ and $\mathbf{P}_{i,j}$. Then $\mathbf{U}_{i,j}$ consists of the image of $(1/2, 1) \times (0, 1)$ under the mapping for $\mathbf{P}_{i-1,j}$ and the image of $(0, 1/2) \times (0, 1)$ under the mapping for $\mathbf{P}_{i,j}$. In Figure 2.4, volume $\mathbf{U}_{i,j}$ is the shaded region.

We associate this volume with the 'vertical' edge shared by $\mathbf{P}_{i-1,j}$ and $\mathbf{P}_{i,j}$, which the control volume straddles. We also have control volumes associated with 'horizontal' edges. For adjacent grid cells, $\mathbf{P}_{i,j-1}$ and $\mathbf{P}_{i,j}$, volume $\mathbf{V}_{i,j}$ consists of the image of $(0, 1) \times (1/2, 1)$ under the mapping for $\mathbf{P}_{i,j-1}$ and the image of $(0, 1) \times (0, 1/2)$ under the mapping for $\mathbf{P}_{i,j}$.

We now need to find a method to generalize the integrations of Section 1.1 that led to the discrete form of Darcy's law. It is worthwhile to summarize what we did there, but now interpreting it from a vector point of view. We

Figure 2.4: **U** Volume

took the x-component of Darcy's law and integrated it over the \mathbf{U} volumes, which is equivalent to taking the dot product of the Darcy law equation with the vector $(1,0)$ and integrating the result over the \mathbf{U} volumes. In equation (1.7), we were able to integrate out the $\frac{\partial\phi}{\partial x}$ term, leaving integrals of ϕ along lines interior to the \mathbf{P} volumes. Because ϕ^h was piecewise constant on \mathbf{P} volumes, in equation (1.8) we could evaluate the line integrals in terms of the nodal values for ϕ^h . For general quadrilaterals, we need to find a suitable vector field, with which to dot Darcy's equation, that allows us to integrate out derivatives of ϕ , leaving integrals that can be evaluated in terms of the nodal values of ϕ^h . Generally a variable vector field will be required because no single constant vector will produce the desired result. Fortunately, simply scaling the vector field \mathbf{X} yields the desired property. We illustrate this process by obtaining the discrete Darcy equation associated with the \mathbf{U} volume shown in Figure 2.4. We proceed first by taking the dot product of equation (2.2) with $c_l\mathbf{X}(x,y)$ and integrating over the 'left half' of $\mathbf{U}_{i,j}$. Similarly, we take the dot product of equation (2.2) with $c_r\mathbf{X}(x,y)$ and integrate over the 'right half' of $\mathbf{U}_{i,j}$. Here, c_l and c_r are constants chosen to eliminate terms involving values of ϕ on the interface between the two halves where ϕ^h is undefined. We then add the two integrals to get our final result. The details of the necessary integrations are in Section 3.2; we will present here only the form of the equation which this integration gives rise to. Note that we perform the same kind of integration for the \mathbf{V} volumes, only we

take the dot product of Darcy’s law with a scaling of the vector \mathbf{Y} . For the \mathbf{U} volume shown in Figure 2.4, we get a discrete Darcy equation relating the pressure drop between the two cells to the fluxes on cell edges:

$$\begin{aligned} & c_1 u_{i-1,j} + c_2 u_{i,j} + c_3 u_{i+1,j} \\ & + c_4 v_{i-1,j} + c_5 v_{i-1,j+1} + c_6 v_{i,j} + c_7 v_{i,j+1} \\ & + |E|(\phi_{i,j} - \phi_{i-1,j}) = 0, \end{aligned}$$

where $|E|$ is the length of the edge shared by the two adjacent grid cells. The values of the coefficients c_1, \dots, c_7 depend on the position of the vertices defining the two grid cells and on the values of the diffusion coefficient within the two cells. Note that the structure of connections here is the same as that obtained for the uniform grid case with tensor permeability in Section 3.1. The ‘cross’ terms c_4, \dots, c_7 will generally be nonzero even when the diffusion coefficient \mathbf{A} is diagonal.

2.2 Multilevel Solvers

2.2.1 FVE Based Multigrid

In this section, we discuss the changes in the multigrid algorithm presented in Section 1.2 needed to deal with general quadrilateral grids. Because the mixed FVE discretization for general quadrilaterals is simply an extension of the discretization for uniform grids, only slight modifications to this algorithm must be made. Given a logically rectangular grid of irregular quadrilaterals, one can generate a finer grid of the same type by dividing each quadrilateral in the given grid into four quadrilaterals. This division is done

by connecting midpoints of opposite sides. In this way, a sequence of finer grids can be generated from a given coarse grid. Figure 2.5 shows a coarse grid Ω^1 and its first refinement Ω^2 . On each of the grids $\Omega^1, \dots, \Omega^N$, we apply the mixed FVE discretization technique of the previous section. Then we can use a multigrid algorithm to generate a solution to the FVE discretization of the problem on the finest grid Ω^N .

The basic components of the multigrid algorithm remain virtually unchanged. Now, because the structure of the connections in the discrete equations remain unchanged, any of the relaxation techniques discussed in Section 1.2 can be used. As was the case for uniform grids, the interpolation operators used in the multigrid algorithm are defined on the basis of the relationship between finite element spaces for the unknowns on different grids. The finite element spaces are still nested, as we show in Section 3.3. The relationship between the finite element spaces for ϕ is the same as in the uniform grid case, so the interpolation operator for ϕ remains unchanged. However, the relationship between the coarse and fine finite element spaces for both u and v is changed somewhat, because these variables now represent fluxes rather than velocities as before. Since the edge of a fine grid cell is half the length of the edge of the corresponding coarse grid cell, the interpolation operators for u and v of Section 1.2 must be scaled by $1/2$.

Again, the restriction operators used in the multigrid algorithm are defined on the basis of the relationship between control volumes on different

Figure 2.5: Ω^1 and Its First Refinement Ω^2

grids. The control volumes for the continuity equation are related in the same way as in the uniform grid case (one coarse grid \mathbf{P} volume consists of four fine grid \mathbf{P} volumes), and so the restriction operator for this equation remains unchanged. The relationship between coarse and fine control volumes for Darcy's equation can be different than it was in the uniform grid case. A coarse grid \mathbf{U} volume contains all of two of the fine grid \mathbf{U} volumes and fractions (no longer necessarily half) of four others. Figure 2.6 depicts the relationship between coarse and fine control volumes. Strict adherence to the FVE principles requires the calculation of the fraction of a fine grid control volume included in the coarse grid control volume; however, we have chosen to use the same restriction operator as in the uniform grid case. It is certainly possible to calculate the fractions and use them in the definition of the restriction operator, but, for the present, we have used this more easily implemented definition (approximating the fractions by $\frac{1}{2}$). From our experience with numerical testing of the algorithm, this approximation does not appear to adversely affect the convergence of the multigrid algorithm. In fact, because the convergence factors are generally quite small, it is not clear that there is much to be gained by stricter adherence to the FVE principles in defining the restriction operator.

Note that in the multigrid algorithm presented here, the process of developing its components begins with the coarsest grid. Input to the algorithm is a coarse grid that models the large-scale irregularities of the reservoir ge-

Figure 2.6: Coarse and Fine Darcy Volumes

ometry, and a specified level of refinement necessary to resolve the flow. The algorithm then generates a solution to the mixed FVE discretization on the finest grid. If a direct method is used to solve the equations on the coarsest grid, then this places a practical limitation on the number of quadrilaterals used to model the reservoir geometry.

2.2.2 A Two-Level Approach

There are two practical problems with the multigrid algorithm discussed in the previous section. The first is that, as in the uniform grid case, the jumps in the diffusion coefficient must occur (if at all) at grid edges on the coarse grid. The second is that the grid irregularity is constructed based on a given coarse grid, which is then refined by bilinear coordinates to generate finer grids: one cannot apply the multigrid algorithm to the equations on the coarsest grid, so they must be solved some other way. In practice, both of these problems represent limitations on the coarsest grid: it must be fine enough to capture the reservoir geology and the jumps in the diffusion coefficient. This limitation may result in the set of discrete equations on the coarsest grid being too large to solve directly.

The two-level approach described in Section 1.3.3 provides one possible remedy to these two problems. The only component of the two-level algorithm that needs additional discussion for the general quadrilateral case is \tilde{M} , which is the mass matrix that multiplies the discrete fluxes in Darcy's equation. For uniform grids, \tilde{M} is defined by equation (1.9), and since it's

diagonal, we invert it to eliminate the flux variables. In essence, we can use a standard cell-centered finite difference discretization as the ‘coarse’ level for the ‘fine’ level mixed FVE discretization. We would like to do something similar for the case of a general quadrilateral grids. However, one of our motivations for looking at the mixed FVE discretization is that it can be applied in a clear and direct way to general quadrilateral grids, where standard cell-centered finite differences cannot. Unfortunately, an effective cell-centered finite difference scheme for discretization on general quadrilateral grids does not currently exist. However, our demands on this scheme are not very strict because the objective of the discretization on the ‘coarse’ level is simply to correct the solution from the ‘fine’ level mixed FVE discretization, which will serve as our final approximation. In other words, we would like to use the ‘coarse’ level discretization only to accelerate the relaxation process on the ‘fine’ level. For this purpose, our experience shows that equation (1.9) serves as an effective way to define \tilde{M} even in the general quadrilateral case. There are perhaps more sophisticated ways of defining \tilde{M} that we may explore later, but we have found that this simple definition works well for many applications. It is clear that, for very distorted grids, \tilde{M} defined this way will provide a poor approximation to M ; however, we will see in the next section that, for moderately distorted grids, the two-level method works as well as in the uniform grid case.

2.3 Computational Results

2.3.1 Multigrid Performance

This section contains results of numerical experiments designed to test the robustness of the multigrid algorithm of Section 2.2.1. For all problems considered here we used two pre-relaxations and one post-relaxation in the multigrid algorithm. For the first test problem, we used the mixed FVE based multigrid algorithm with a coarsest grid of eight cells in each direction. We began with a uniform 8×8 grid on $\Omega = [-1, 1] \times [-1, 1]$ and then moved each interior vertex in both the x and y direction separately by a random number between $-.2h$ and $.2h$, where the original mesh size is $h = .25$. The resulting grid is shown in Figure 2.7.

We then solved the mixed FVE discretization of Poisson's equation, where the diffusion coefficient is the identity, using the multigrid algorithm of Section 2.2 with varying levels of refinement. Ten or more cycles were performed on the homogeneous problem and the average convergence factor was calculated. The results are shown below.

Grid Size	Convergence Factor
16×16	.12
32×32	.17
64×64	.22

Here we used distributive Gauss-Seidel relaxation and we see convergence factors that are quite acceptable for this distorted grid in that they are relatively small, do not grow significantly with problem size, and are not much

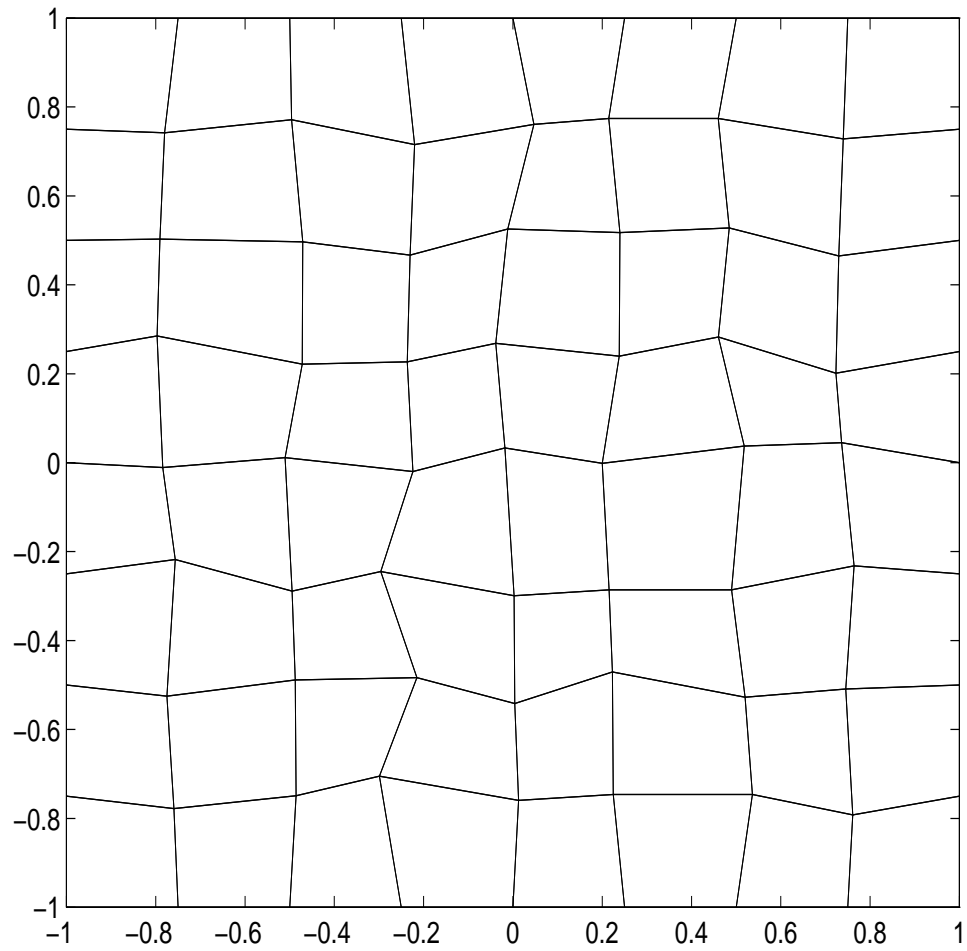


Figure 2.7: Grid with up to 20% Distortion

different from the convergence factors for the uniform grid case. The algorithm allows us to solve this problem with about as much work as is needed to solve the uniform grid problem.

For the second numerical experiment, we solved the same problem, only now the 8×8 grid was distorted by moving each interior vertex in both the x and y direction by a random number between $-.5h$ and $.5h$. The resulting grid is shown in Figure 2.7.

This grid is likely to be much more distorted than one would encounter in an application, and, in fact, some of the quadrilaterals are no longer convex. The results for the mixed FVE based multigrid algorithm are shown below.

Grid Size	Convergence Factor
16×16	.03
32×32	.05
64×64	.08

Because of the significant distortion of the coarsest grid, we used alternating line relaxation for this test example: analogous to the anisotropic uniform grid case, the structure of the resulting discrete mixed FVE equations consists of cells that are strongly coupled to some neighbors and weakly coupled to others. We need alternating line relaxation to get the error smoothing that is needed for acceptable multigrid convergence factors. With this more expensive algorithm, compared to the cell by cell distributive Gauss-Seidel relaxation, we obtain quite good multigrid convergence factors for this very distorted grid.

The third numerical test combined moderately distorted grids with a

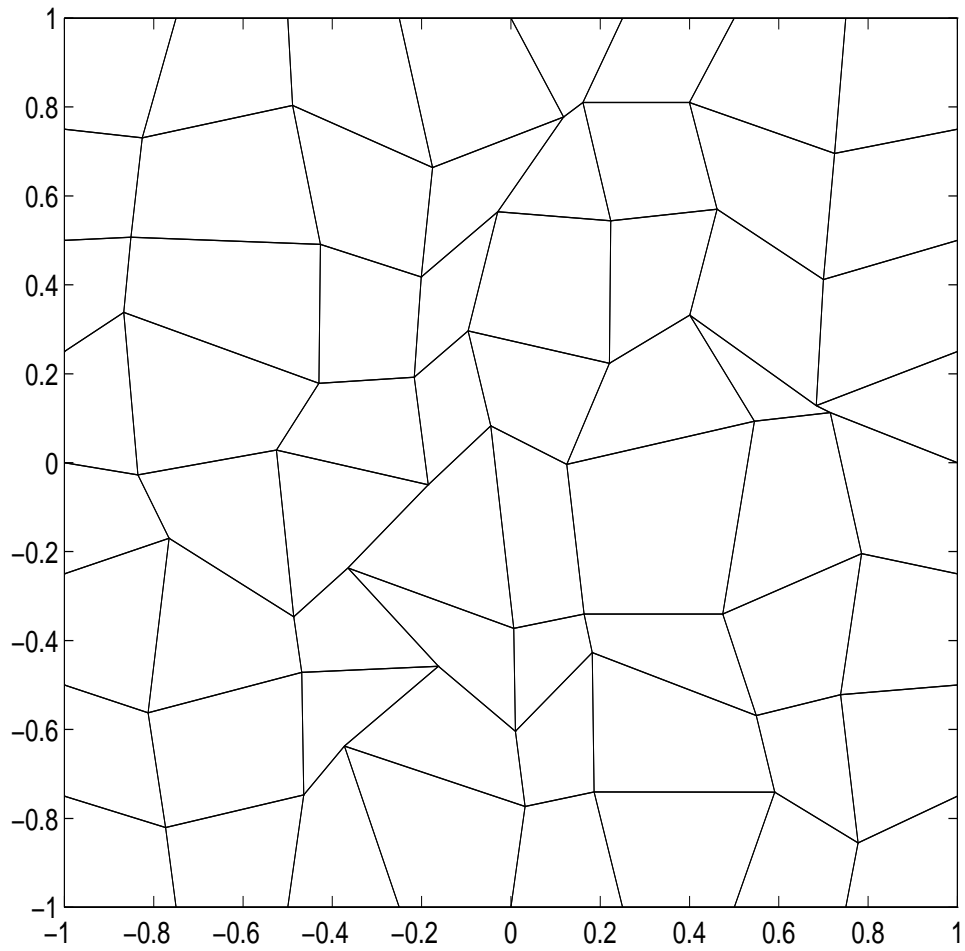


Figure 2.8: Grid with up to 50% Distortion

diagonal but anisotropic and discontinuous diffusion coefficient. The coarsest grid here is the same as that used in the first experiment, an 8×8 grid with up to 20% distortion. On each cell in this coarsest grid the diffusion coefficients a_x and a_y were separately set to random values between .01 and 100. The results for the mixed FVE based multigrid algorithm are shown below.

Grid Size	Convergence Factor
16×16	.04
32×32	.06
64×64	.08

Again we used alternating line relaxation, now because of the anisotropic diffusion coefficient. Again we see quite good multigrid convergence factors. This numerical test is close to the types of problems that might actually occur in an application and the performance of the multigrid algorithm is well within an acceptable range.

The two restrictions on the coarsest grid for our mixed FVE based multigrid method that were discussed in Section 2.2.2, namely, capturing the irregularity and discontinuities of the diffusion coefficient, have not been violated in the numerical experiments thus far. However, even without violating these limitations, one can pose problems where the mixed FVE based multigrid method fails to perform as well as in the above tests. For example, consider the coarsest grid used in second numerical experiment: 8×8 with up to 50% distortion. On each cell in this grid, the diffusion coefficients a_x and a_y were separately set to random values between $1/a$ and a . The results for the mixed FVE based multigrid algorithm using four grids (finest grid is

64×64) are shown below.

a	Convergence Factor
1	.08
10	.13
100	.15
1000	.20

These last results may be of little practical interest as the grid is much more distorted than one would likely use in an application, but they do demonstrate the robustness of the multigrid algorithm. For all numerical tests encountered thus far, the mixed FVE based multigrid algorithm with alternating line relaxation has yielded acceptable (rarely worse than .3) convergence factors if the lines of discontinuity in the diffusion coefficient are captured on the coarsest grid. With full tensor coefficients, when the anisotropy is not aligned with the coordinates, the convergence factors can be significantly larger (at times, as large as .6), and we have no rigorous theoretical results, so we can make no general claims. However, it appears that the method has potential as a fast solver in many important practical applications.

2.3.2 Two-Level Performance

This section contains results of numerical tests designed to test the robustness of the two-level approach of Section 2.2.2. This is an approach that one could use alone or as the coarsest grid solver in the mixed FVE based multigrid. For the results of this section, we use alternating line relaxation, with two sweeps

performed before solving the ‘coarse’ problem and one sweep performed after. Five cycles of black box multigrid were used to solve the ‘coarse’ problem, although often two or three are sufficient. In the first numerical experiment, the mixed FVE discretization of Poisson’s equation on $\Omega = [-1, 1] \times [-1, 1]$ was solved on the moderately distorted grid obtained from a uniform grid by the up to 20% distortion described in the previous section. Note that the distortion here takes place on the finest grid, so the mixed FVE based multigrid algorithm cannot be used. Average convergence factors for the two-level approach on different size grids are shown below.

Grid Size	Convergence Factor
16 × 16	.07
32 × 32	.08
64 × 64	.08

The convergence factors are remarkably good, given the quality of the approximation used on the ‘coarse’ level. As discussed in Section 2.2.2, we basically assume the grid is uniform in constructing the mass matrix \tilde{M} for the discrete Darcy equations on the ‘coarse’ level. This appears to work well for the moderately distorted grids like those in this numerical experiment and, quite probably, the grids one would use in practical applications. When the grid is very distorted, like the up to 50% distorted grid of the previous section, the two-level algorithm can fail to converge and may even diverge. The reason is that the very poor approximation of the mass matrix results in a correction from the ‘coarse’ level that has little, if anything, to do with the ‘fine’ level error. It is possible that this could be remedied by a more

sophisticated choice for \tilde{M} , but this has yet to be investigated.

In the next numerical experiment, we use the same grids as in the previous test and solve the mixed FVE discretization to the diffusion equation with diagonal diffusion coefficient, where on each cell in this grid the diffusion coefficients a_x and a_y were separately set to random values between .01 and 100. The results, in terms of average convergence factors, are shown below.

Grid Size	Convergence Factor
16 × 16	.43
32 × 32	.40
64 × 64	.38

While the convergence factors are not as small as for Poisson-like problems, they are likely acceptable in most practical applications, especially if one is using the two-level approach only on the coarsest grid of the mixed FVE based multigrid algorithm. There the amount of work on finer grids in the mixed FVE based multigrid algorithm will typically be much larger than the work of the two-level algorithm on the coarsest grid, even if several cycles of the two-level algorithm are required. We should note that the convergence factors for this problem are roughly equal to those obtained for the similar uniform grid problem: our belief is that the “poor” convergence factors are again due to the difference between the mixed FVE method’s and the finite difference method’s treatment of discontinuities in \mathbf{A} , not related to the moderate irregularity of the grid.

2.3.3 Accuracy of the Mixed FVE Discretization

In this section, we present results of numerical experiments to investigate the accuracy of the mixed FVE discretization on general quadrilateral grids.

First, we will present the result of a simple numerical test designed to illustrate the effect that the shape of the grid cells has on discretization errors and multigrid convergence rates. We consider Poisson's equation posed on $\Omega = [-1, 1]^2$:

$$\begin{aligned}\mathbf{v} + \nabla\phi &= 0, \\ \nabla \cdot \mathbf{v} &= f,\end{aligned}$$

with boundary condition $\mathbf{v} \cdot \boldsymbol{\eta} = g$. For this test, f and g were determined so that the exact solution is,

$$\phi(x, y) = \cos(\pi x) \cos(2\pi y) + \text{constant}.$$

The solution from the mixed FVE discretization was normalized to correspond the exact solution with constant= 0. The coarsest grid we use in our tests is shown in Figure 2.9.

To investigate the effect of the angle β on the accuracy of the mixed FVE discretization and on multigrid convergence factors, we use varying β . We measure the error in the same way as in Section 1.3, using the \mathcal{L}^2 norm of the ϕ error and ℓ^2 norm of the u and v errors. In the tables below, we compile our observations on these errors and the average convergence factors for the mixed FVE based multigrid algorithm. For $\beta = 80^\circ$ and 70° , distributive Gauss-Seidel relaxation proved effective in terms of convergence factors. For

Figure 2.9: Coarsest Grid

$\beta = 60^\circ$ and 50° , the stronger alternating line relaxation scheme was needed to get acceptable convergence factors. This is again due to the distortion of the grids that yield couplings of different strengths to neighboring cells.

$\beta = 80^\circ$ distributive Gauss-Seidel				
Fine Grid	ϕ_e	u_e	v_e	Convergence Factor
8×8	4.841E-1	1.575E-1	7.595E-2	.054
16×16	2.514E-1	5.090E-2	2.538E-2	.073
32×32	1.267E-1	1.347E-2	6.752E-3	.083
64×64	6.354E-2	3.414E-3	1.713E-3	.086

$\beta = 70^\circ$ distributive Gauss-Seidel				
Fine Grid	ϕ_e	u_e	v_e	Convergence Factor
8×8	4.881E-1	2.327E-1	1.106E-1	.067
16×16	2.541E-1	6.541E-2	3.330E-2	.090
32×32	1.285E-1	1.689E-2	8.809E-3	.107
64×64	6.516E-2	4.256E-3	2.235E-3	.143

$\beta = 60^\circ$ alternating line relaxation				
Fine Grid	ϕ_e	u_e	v_e	Convergence Factor
8×8	5.009E-1	3.506E-1	2.140E-1	.019
16×16	2.619E-1	9.111E-2	5.723E-2	.031
32×32	1.335E-1	2.305E-2	1.483E-2	.035
64×64	6.967E-2	5.779E-3	3.745E-3	.054

$\beta = 50^\circ$ alternating line relaxation				
Fine Grid	ϕ_e	u_e	v_e	Convergence Factor
8×8	5.318E-1	6.060E-1	4.169E-1	.022
16×16	2.760E-1	1.737E-1	1.199E-1	.038
32×32	1.406E-1	4.493E-2	3.189E-2	.057
64×64	7.382E-2	1.135E-2	8.142E-3	.097

These results, show good convergence in the accuracy of the discretization as the grids are refined. Each refinement reduces the norm of the error in ϕ by a factor of 2 and the error in the fluxes by a factor of 4. Although

we do not have rigorous proofs of the order of convergence of the mixed FVE discretization, these results, and all other results from experiments with analytic solutions, appear to indicate that, at least in the norms we used, the convergence is first order in the pressure and second order in the fluxes. We also see that the accuracy of the discretization decreases as β decreases, which is not surprising since most finite element approximations degrade as the grid becomes less uniform. However, one can still likely achieve a solution of any practical accuracy by refining the grid yet further. Note also that the multigrid convergence factors degrade slightly as the grid becomes less uniform, but the factors are still certainly acceptable.

The next problem is similar to the previous one in that the same type of grids are used, and the boundary condition and right hand side were determined so that it has the same exact solution; however, this problem has full tensor permeability. The diffusion coefficient \mathbf{A} is given by

$$\mathbf{A} = \begin{pmatrix} \cos \theta & \sin \theta \\ -\sin \theta & \cos \theta \end{pmatrix} \begin{pmatrix} 1 & 0 \\ 0 & 0.01 \end{pmatrix} \begin{pmatrix} \cos \theta & -\sin \theta \\ \sin \theta & \cos \theta \end{pmatrix},$$

where θ , the angle between the coordinate axes and the principal directions of permeability, is 45° . The errors in the mixed FVE approximations for various size grids and varying angle of distortion β are given below:

$\beta = 80^\circ$			
Fine Grid Size	ϕ_e	u_e	v_e
16×16	2.261	2.722E-1	1.998E-1
32×32	0.6356	9.497E-2	7.194E-2
64×64	0.1743	2.714E-2	2.078E-2
128×128	0.0520	7.042E-3	5.442E-3

$\beta = 60^\circ$			
Fine Grid Size	ϕ_ϵ	u_ϵ	v_ϵ
16×16	3.092	4.527E-1	3.021E-1
32×32	0.9468	1.963E-1	1.398E-1
64×64	0.2698	6.375E-2	4.568E-2
128×128	0.0788	1.747E-2	1.267E-2

As in the uniform grid case, the accuracy degrades due to the anisotropy not being aligned with the coordinates, but the results still indicate second-order convergence in the velocities. Note that for $\beta = 60^\circ$ and $\theta = 45^\circ$, a case with severe distortion and non-grid aligned anisotropy, the asymptotic regime is not reached until the grid is quite fine.

The final test problem involves a non-uniform grid and full tensor, discontinuous permeability. The domain for the problem, which consists of three regions, is depicted in Figure 2.10.

The coefficient \mathbf{A} is defined in each region as follows:

$$\begin{array}{ccc}
 \text{In region I} & \text{In region II} & \text{In region III} \\
 \begin{pmatrix} \frac{1}{4} & \frac{1}{4} \\ \frac{1}{4} & 4 \end{pmatrix} & \begin{pmatrix} 2 & 1 \\ 1 & 1 \end{pmatrix} & \begin{pmatrix} 2 & \frac{1}{2} \\ \frac{1}{2} & \frac{1}{2} \end{pmatrix}
 \end{array}$$

The boundary conditions and right hand side were defined so that the exact solution is given by,

$$\begin{array}{ccc}
 \text{In region I} & \text{In region II} & \text{In region III} \\
 \phi = x^2 + C & \phi = \frac{1}{16}y^2 + C & \phi = \frac{1}{4}y^2 + C
 \end{array}$$

Again the value of C is chosen to correspond to the solution whose integral over the domain vanishes. Note that, ϕ and the normal component of $\mathbf{A}\nabla\phi$ are continuous across the interfaces between regions. The coarsest grid (a

Figure 2.10: Problem Domain

2×2 grid), was formed by splitting, along the x -axis, region **I** into two cells, and all finer grids were generated by bilinear refinement of this coarsest grid. The errors in the mixed FVE approximation, calculated in the same way as previously, are presented in the table below.

Grid Size	ϕ_ϵ	u_ϵ	v_ϵ
4×4	0.2524	7.065E-3	8.269E-3
8×8	0.1302	1.747E-3	2.197E-3
16×16	0.0658	4.567E-4	5.859E-4
32×32	0.0333	1.213E-4	1.582E-4
64×64	0.0174	3.234E-5	4.294E-5

Here we clearly see first-order convergence in the pressure, and again we see second-order convergence in the velocities, which has been the case for all experiments, ranging from Poisson's equation on a uniform grid to this significantly more complicated case, with analytic solutions.

3 Technical Derivations

This chapter contains all the derivations needed to assemble the mixed FVE equations. Many of the results from this section have been briefly presented, or at least alluded to, in previous sections.

3.1 Uniform Grids and Tensor Permeability

In Section 1.1, we presented the FVE discretization assuming that the coefficient \mathbf{A} in equation (1.1) is a diagonal tensor. Here we consider the case where \mathbf{A} is a full tensor, but we assume that it is a pointwise symmetric, positive definite matrix. In this section, we assume the grid is uniform (see the following section for the general quadrilateral case). We write

$$\mathbf{A} = \begin{pmatrix} a & b \\ b & c \end{pmatrix},$$

where a, b , and c may now be functions of position. Darcy's law, equation (1.2), takes the form

$$\mathbf{v} = -\mathbf{A}\nabla\phi,$$

or

$$\mathbf{A}^{-1}\mathbf{v} + \nabla\phi = 0.$$

Now, adding the conservation of mass equation and noting that $\mathbf{v} = (u, v)^t$, we have the following first-order system:

$$\begin{cases} (\det \mathbf{A})^{-1} (cu - bv) + \partial\phi/\partial x = 0 & \text{(u equation)} \\ (\det \mathbf{A})^{-1} (-bu + av) + \partial\phi/\partial y = 0 & \text{(v equation)} \\ \partial u/\partial x + \partial v/\partial y = f & \text{(p equation)}. \end{cases} \quad (3.1)$$

The main components of the mixed FVE discretization process remain the same: the choice of volumes and finite element spaces are the same as presented in Section 1.1. The change in the form of the u equation, comparing equation (3.1) to equation (1.4), is reflected when we integrate the u equation over the \mathbf{U} volumes. In this section, we will assume that \mathbf{A} is constant over the integration domain, otherwise the technique of Section 3.3 can be applied. As an example, let $\mathbf{U}_{i,j}$ be the volume in \mathcal{U} that is centered at the interior u^h node (i, j) as shown in Figure 3.1.

We then have

$$\int_{\mathbf{U}_{i,j}} \left((\det \mathbf{A})^{-1} (cu - bv) + \partial\phi/\partial x \right) dx dy = 0. \quad (3.2)$$

Integration of the terms involving u and $\partial\phi/\partial x$ is the same as in Section 1.1. The additional term involving v is handled by splitting the integral into two parts, one for each half of $\mathbf{U}_{i,j}$. Then, because our finite element approximation v^h is linear in y and constant in x on each half, by direct calculation of

Figure 3.1: **U** Volume

the integral over the left half, we have

$$\int_{\mathbf{U}_{i,j}^l} v dx dy = \frac{h^2}{4} (v_{i-1,j+1}^h + v_{i-1,j}^h).$$

Combining this result with the analogous one for the other half and adding the results from Section 1.1 for the other terms in equation (3.2), we get the discrete equation

$$\begin{aligned} & \frac{h^2}{8} (c(\det \mathbf{A})^{-1}) (u_{i-1,j}^h + 6u_{i,j}^h + u_{i+1,j}^h) \\ & - \frac{h^2}{4} (b(\det \mathbf{A})^{-1}) (v_{i-1,j+1}^h + v_{i-1,j}^h + v_{i,j+1}^h + v_{i,j}^h) \\ & + h (\phi_{i,j}^h - \phi_{i-1,j}^h) = 0. \end{aligned}$$

We get a similar equation when we integrate over \mathbf{V} volumes. This change in the form of the discrete Darcy law is the only change in the discretization process from Section 1.1.

3.2 Derivation of FVE Stencils for General Quadrilaterals

3.2.1 Scalar Diffusion Coefficient

Here we develop the details of the integrals encountered in deriving the discrete Darcy equation for general quadrilateral grids. We first consider the case where the diffusion coefficient is a scalar. The case where the diffusion coefficient is a tensor is covered in Section 3.2.2. Shown in Figure 3.2 by dotted lines is a typical \mathbf{U} volume, which we will use to discretize Darcy's equation.

Figure 3.2: **U** Volume

\mathbf{P}_l and \mathbf{P}_r will denote the two P volumes who share the edge with which the U volume is associated. The continuous Darcy equation is

$$a^{-1}\mathbf{v}(x, y) + \nabla\phi(x, y) = 0. \quad (3.3)$$

As mentioned in Section 2.1, we take the dot product of equation (3.3) with $c_l\mathbf{X}(x, y)$ and integrate over the ‘left half’ of the U volume. Similarly, we take the dot product of equation (3.3) with $c_r\mathbf{X}(x, y)$ and integrate over the ‘right half’ of the U volume. We then add the two integrals to get the discrete Darcy equation corresponding to this U volume. Letting \mathbf{U}_l and \mathbf{U}_r denote the two ‘halves’ of the U volume, we have the following:

$$\begin{aligned} & \int_{\mathbf{U}_l} (a^{-1}\mathbf{v}(x, y) + \nabla\phi(x, y)) \cdot c_l\mathbf{X}(x, y) dx dy + \\ & \int_{\mathbf{U}_r} (a^{-1}\mathbf{v}(x, y) + \nabla\phi(x, y)) \cdot c_r\mathbf{X}(x, y) dx dy = \end{aligned} \quad (3.4)$$

$$\begin{aligned} & c_l \int_{\mathbf{U}_l} a^{-1}\mathbf{v}(x, y) \cdot \mathbf{X}(x, y) dx dy + c_l \int_{\mathbf{U}_l} \nabla\phi(x, y) \cdot \mathbf{X}(x, y) dx dy + \\ & c_r \int_{\mathbf{U}_r} a^{-1}\mathbf{v}(x, y) \cdot \mathbf{X}(x, y) dx dy + c_r \int_{\mathbf{U}_r} \nabla\phi(x, y) \cdot \mathbf{X}(x, y) dx dy. \end{aligned}$$

Thus, we have two types of integrals to evaluate, ones involving \mathbf{v} and ones involving $\nabla\phi$.

First consider the integral involving \mathbf{v} . For the moment, we ignore the scaling parameters c_l and c_r . We evaluate this integral for the finite element basis functions for \mathbf{v} , which are the formulas needed to assemble the stencil for equation (3.4). Consider the evaluation of

$$\int_{U_l} a^{-1}\mathbf{w}(x, y) \cdot \mathbf{X}(x, y) dx dy,$$

where \mathbf{w} is the basis function with flux equal to 1 on the edge straddled by the U volume and 0 on all other grid edges. It is important to recall the

properties used to define our finite element space: within each grid cell,

$$\begin{aligned} \mathbf{w}(x, y) \cdot \eta_x(x, y) \|\mathbf{Y}(x, y)\| & \text{ varies linearly with } \hat{x}, \text{ constant with } \hat{y}, \\ \mathbf{w}(x, y) \cdot \eta_y(x, y) \|\mathbf{X}(x, y)\| & \text{ varies linearly with } \hat{y}, \text{ constant with } \hat{x}. \end{aligned} \tag{3.5}$$

The first condition implies, that within the volume \mathbf{P}_l ,

$$\mathbf{w}(x, y) \cdot \eta_x(x, y) \|\mathbf{Y}(x, y)\| = \hat{x},$$

where \hat{x} refers to the pre-image of x in the reference space. Similarly, \hat{y} will denote the pre-image of y in the reference space. The second condition, along with the fact that fluxes are zero on the top and bottom edges of \mathbf{P}_l , implies that, within the volume \mathbf{P}_l , we have

$$\mathbf{w}(x, y) \cdot \eta_y(x, y) \|\mathbf{X}(x, y)\| = 0.$$

Thus, \mathbf{w} is perpendicular to η_y and, hence, parallel to \mathbf{X} . We thus have,

$$\mathbf{w}(x, y) \cdot \mathbf{X}(x, y) = \|\mathbf{w}(\mathbf{x}, \mathbf{y})\| \|\mathbf{X}(\mathbf{x}, \mathbf{y})\|$$

and

$$\mathbf{w}(x, y) \cdot \eta_x(x, y) = \|\mathbf{w}(\mathbf{x}, \mathbf{y})\| \sin(\theta(\mathbf{x}, \mathbf{y})),$$

where θ is the angle between \mathbf{X} and \mathbf{Y} as shown in Figure 3.2. Solving this last equation for the norm, we get

$$\|\mathbf{w}(x, y)\| = (\mathbf{w}(x, y) \cdot \eta_x(x, y)) / \sin(\theta(x, y)). \tag{3.6}$$

Putting these results together, we have,

$$\begin{aligned}
& \int_{\mathbf{U}_l} a^{-1} \mathbf{w}(x, y) \cdot \mathbf{X}(x, y) dx dy \\
&= \int_{\mathbf{U}_l} a^{-1} \|\mathbf{w}(x, y)\| \|\mathbf{X}(x, y)\| dx dy \\
&= \int_{\mathbf{U}_l} a^{-1} ((\mathbf{w}(x, y) \cdot \boldsymbol{\eta}_x(x, y)) / \sin(\theta(x, y))) \|\mathbf{X}(x, y)\| dx dy \\
&= \int_0^1 \int_{\frac{1}{2}}^1 a^{-1} \hat{x} \|\mathbf{X}(\hat{x}, \hat{y})\|^2 d\hat{x} d\hat{y}.
\end{aligned} \tag{3.7}$$

The last step is the result of the change of variables from the actual space to the reference space. The Jacobian for the map is

$$J = \|\mathbf{X}\| \|\mathbf{Y}\| \sin \theta.$$

This final integral can now be evaluated analytically in the reference space.

We had defined the vector field $\mathbf{X}(x, y)$ by taking images of the unit vector $(1, 0)$ under the bilinear mapping

$$\begin{aligned}
x(\hat{x}, \hat{y}) &= x_{00} + (x_{10} - x_{00})\hat{x} + (x_{01} - x_{00})\hat{y} + (x_{11} - x_{10} - x_{01} + x_{00})\hat{x}\hat{y}, \\
y(\hat{x}, \hat{y}) &= y_{00} + (y_{10} - y_{00})\hat{x} + (y_{01} - y_{00})\hat{y} + (y_{11} - y_{10} - y_{01} + y_{00})\hat{x}\hat{y}.
\end{aligned}$$

We can express the vector field \mathbf{X} as follows:

$$\begin{aligned}
\mathbf{X} &= (\partial x / \partial \hat{x}, \partial y / \partial \hat{x}) \\
&= ((x_{10} - x_{00}) + (x_{11} - x_{10} - x_{01} + x_{00})\hat{y}, \\
&\quad (y_{10} - y_{00}) + (y_{11} - y_{10} - y_{01} + y_{00})\hat{y}).
\end{aligned} \tag{3.8}$$

Thus, the last integrand in equation (3.7) is a polynomial in \hat{x} and \hat{y} whose coefficients depend on the coordinates of the vertices of \mathbf{P}_l , and this integral can easily be evaluated analytically.

Next consider the evaluation of

$$\int_{U_l} a^{-1} \mathbf{w}(x, y) \cdot \mathbf{X}(x, y) dx dy,$$

where \mathbf{w} is the basis function with flux equal to 1 on the top edge of the left grid cell and 0 on all other grid edges. The second condition in (3.5) implies that, within the volume \mathbf{P}_l , we have

$$\mathbf{w}(x, y) \cdot \eta_y(x, y) \|\mathbf{X}(x, y)\| = \hat{y}.$$

The first condition in equation (3.5), along with the fact that the fluxes are zero on the left and right edges of \mathbf{P}_l , implies that, within the volume \mathbf{P}_l , we have

$$\mathbf{w}(x, y) \cdot \eta_x(x, y) \|\mathbf{Y}(x, y)\| = 0.$$

Thus, \mathbf{w} is perpendicular to η_x and, hence, parallel to \mathbf{Y} . We thus have,

$$\mathbf{w}(x, y) / \|\mathbf{w}(x, y)\| = \mathbf{Y}(x, y) / \|\mathbf{Y}(x, y)\|$$

and

$$\mathbf{w}(x, y) \cdot \eta_y(x, y) = \|\mathbf{w}(x, y)\| \sin(\theta(x, y)).$$

Solving this last equation for the norm, we get

$$\|\mathbf{w}(x, y)\| = (\mathbf{w}(x, y) \cdot \eta_y(x, y)) / \sin(\theta(x, y)). \quad (3.9)$$

Putting these results together, we have,

$$\begin{aligned} & \int_{\mathbf{U}_l} a^{-1} \mathbf{w}(x, y) \cdot \mathbf{X}(x, y) dx dy \\ &= \int_{\mathbf{U}_l} a^{-1} \|\mathbf{w}(x, y)\| (\mathbf{w}(x, y) / \|\mathbf{w}(x, y)\|) \cdot \mathbf{X}(x, y) dx dy \\ &= \int_{\mathbf{U}_l} a^{-1} ((\mathbf{w}(x, y) \cdot \eta_y(x, y)) / \sin(\theta(x, y))) \\ & \quad \cdot (\mathbf{Y}(x, y) / \|\mathbf{Y}(x, y)\|) \cdot \mathbf{X}(x, y) dx dy \\ &= \int_0^1 \int_{\frac{1}{2}}^1 a^{-1} \hat{y} \mathbf{X} \cdot \mathbf{Y} d\hat{x} d\hat{y} \end{aligned} \quad (3.10)$$

Again, the last step is a result of the change of variables. This integral can now be evaluated analytically in the reference space. The vector field \mathbf{Y} can be written in terms of reference space coordinates as follows:

$$\begin{aligned}\mathbf{Y} &= (\partial x / \partial \hat{y}, \partial y / \partial \hat{y}) \\ &= ((x_{01} - x_{00}) + (x_{11} - x_{10} - x_{01} + x_{00})\hat{x}, \\ &\quad (y_{01} - y_{00}) + (y_{11} - y_{10} - y_{01} + y_{00})\hat{x}).\end{aligned}\tag{3.11}$$

Thus, the last integrand in equation (3.10) is a polynomial in \hat{x} and \hat{y} whose coefficients depend on the coordinates of the vertices of \mathbf{P}_l , and this integral can easily be evaluated analytically. Integrals for other basis functions are analogous to one of the two that we presented because they can be evaluated in the same way with a simple change of variables. The basis functions that will have nonzero contribution to the integral

$$\int_{\mathbf{U}_l} a^{-1} \mathbf{w}(x, y) \cdot \mathbf{X}(x, y) dx dy$$

will be those that are associated with one of the edges of either \mathbf{P}_l or \mathbf{P}_r . There are seven such edges, so the discrete version of Darcy's law on the volume \mathbf{U} will involve seven nodal values for fluxes.

Now consider the terms involving $\nabla \phi$, for example,

$$\int_{\mathbf{U}_l} \nabla \phi(x, y) \cdot \mathbf{X}(x, y) dx dy.$$

We again express \mathbf{X} in of terms reference space variables to get

$$\begin{aligned}
& \int_{\mathbf{U}_l} \nabla \phi(x, y) \cdot \mathbf{X}(x, y) dx dy \\
&= \int_{\mathbf{U}_l} (\partial \phi / \partial x, \partial \phi / \partial y) \cdot (\partial x / \partial \hat{x}, \partial y / \partial \hat{x}) dx dy \\
&= \int_{\mathbf{U}_l} \frac{\partial \phi}{\partial x} \frac{\partial x}{\partial \hat{x}} + \frac{\partial \phi}{\partial y} \frac{\partial y}{\partial \hat{x}} dx dy \tag{3.12} \\
&= \int_{\mathbf{U}_l} \partial \phi / \partial \hat{x} dx dy \\
&= \int_0^1 \int_{\frac{1}{2}}^1 \frac{\partial \phi}{\partial \hat{x}} J d\hat{x} d\hat{y}.
\end{aligned}$$

Here, J is again the Jacobian of the mapping, which can be expressed as

$$J = \frac{\partial x}{\partial \hat{x}} \frac{\partial y}{\partial \hat{y}} - \frac{\partial x}{\partial \hat{y}} \frac{\partial y}{\partial \hat{x}}.$$

Note that, expressed in terms of reference space variables, we have

$$J(\hat{x}, \hat{y}) = a + b\hat{x} + c\hat{y},$$

where a, b , and c are constants on the quadrilateral \mathbf{P}_l and depend on the location of its vertices. With this and the last result in equation (3.12), we have

$$\begin{aligned}
& \int_{\mathbf{U}_l} \nabla \phi(x, y) \cdot \mathbf{X}(x, y) dx dy \\
&= \int_0^1 \int_{\frac{1}{2}}^1 \frac{\partial \phi}{\partial \hat{x}} J d\hat{x} d\hat{y} \\
&= \int_0^1 \int_{\frac{1}{2}}^1 \left[\frac{\partial}{\partial \hat{x}} (J\phi) - b\phi \right] d\hat{x} d\hat{y} \\
&= \int_0^1 J(1, \hat{y}) \phi(1, \hat{y}) d\hat{y} - \int_0^1 J(\frac{1}{2}, \hat{y}) \phi(\frac{1}{2}, \hat{y}) d\hat{y} - b \int_0^1 \int_{\frac{1}{2}}^1 \phi d\hat{x} d\hat{y}.
\end{aligned}$$

We have now accomplished the goal of integrating out the derivatives of ϕ .

The second integral is a line integral interior to the volume \mathbf{P}_l and can be

written in terms of nodal values of ϕ ; also, the third integral is a volume integral within the volume \mathbf{P}_l and can be written in terms of nodal values of ϕ . Because the approximation of ϕ is constant on \mathbf{P}_1 (constant = $\phi_{i,j}$), for the third integral we have

$$b \int_0^1 \int_{\frac{1}{2}}^1 \phi d\hat{x}d\hat{y} = \frac{b}{2} \phi_{i,j}.$$

However, the first integral is a line integral along the edge shared by \mathbf{P}_l and \mathbf{P}_r , and because we approximate ϕ with a piecewise constant function, we seek to remove the first integral. In terms of the Jacobian of the map for the right grid cell in Figure 3.2, similar integrations over \mathbf{U}_r produces

$$\begin{aligned} \int_{\mathbf{U}_r} \nabla \phi(x, y) \cdot \mathbf{X}(x, y) dx dy = \\ \int_0^1 J(\frac{1}{2}, \hat{y}) \phi(\frac{1}{2}, \hat{y}) d\hat{y} - \int_0^1 J(0, \hat{y}) \phi(0, \hat{y}) d\hat{y} - b \int_0^1 \int_0^{\frac{1}{2}} \phi d\hat{x}d\hat{y}. \end{aligned}$$

In this expression, the first and third integral can be expressed in terms of nodal values of ϕ ; the second integral involves integration along the edge shared by \mathbf{P}_l and \mathbf{P}_r . It is at this point that we see the utility of the scaling parameters c_l and c_r . We choose them so that when we add the results from the two halves, the terms involving ϕ on the interface between the two grid cells cancel. In fact, choosing $c_l = |E|/J(1, \frac{1}{2})$ and $c_r = |E|/J(0, \frac{1}{2})$ gives us the result

$$c_l \int_{\mathbf{U}_l} \nabla \phi(x, y) \cdot \mathbf{X}(x, y) dx dy + c_r \int_{\mathbf{U}_r} \nabla \phi(x, y) \cdot \mathbf{X}(x, y) dx dy = |E|(\phi_{i+1,j} - \phi_{i,j}).$$

Here, $|E|$ is the length of the edge shared by \mathbf{P}_l and \mathbf{P}_r .

3.2.2 Tensor Diffusion Coefficient

For a full tensor coefficient, much of the results from the previous section are unchanged, including, for example, all of the results for the part of the integral involving ϕ . We must only reconsider the evaluation of

$$\int_U \mathbf{A}^{-1} \mathbf{w}(x, y) \cdot \mathbf{X}(x, y) dx dy$$

when \mathbf{w} is one of the two basis functions discussed in the previous section. Again we split the volume into a left and right half and integrate over each half separately. We will use the same notation as in the previous section, so that Figure 3.2 still represents the U volume that we integrate over.

We first consider the case where \mathbf{w} is the basis function that has flux equal to 1 on the edge straddled by the U volume and 0 on all other grid edges. We proceed as follows:

$$\begin{aligned} & \int_{U_l} \mathbf{A}^{-1} \mathbf{w}(x, y) \cdot \mathbf{X}(x, y) dx dy \\ &= \int_{U_l} \mathbf{w}(x, y) \cdot \mathbf{A}^{-T} \mathbf{X}(x, y) dx dy \\ &= \int_{U_l} \|\mathbf{w}(x, y)\| (\mathbf{w}(x, y) / \|\mathbf{w}(x, y)\|) \cdot \mathbf{A}^{-T} \mathbf{X}(x, y) dx dy \\ &= \int_{U_l} ((\mathbf{w}(x, y) \cdot \boldsymbol{\eta}_x(x, y)) / \sin(\theta(x, y))) \\ &\quad \cdot (\mathbf{X}(x, y) / \|\mathbf{X}(x, y)\|) \cdot \mathbf{A}^{-T} \mathbf{X}(x, y) dx dy \\ &= \int_0^1 \int_{\frac{1}{2}}^1 \hat{x} \mathbf{X}(\hat{x}, \hat{y}) \cdot \mathbf{A}^{-T} \mathbf{X}(\hat{x}, \hat{y}) d\hat{x} d\hat{y} \\ &= \int_0^1 \int_{\frac{1}{2}}^1 \hat{x} \mathbf{A}^{-1} \mathbf{X}(\hat{x}, \hat{y}) \cdot \mathbf{X}(\hat{x}, \hat{y}) d\hat{x} d\hat{y}. \end{aligned} \tag{3.13}$$

The first step follows from the adjoint property; the third step uses equa-

tion (3.6) and the fact that \mathbf{w} and \mathbf{X} are parallel; the fourth step is the result of the change of variables to the reference space; and the final step again follows from the adjoint property. We can then evaluate the final integral in equation (3.13) in the reference space using equation (3.8) to express \mathbf{X} in terms of the reference variables. The integrand, as in the previous section, is just a polynomial in \hat{x} and \hat{y} , so this integral can easily be evaluated analytically.

We now consider the case where \mathbf{w} is the basis function that has flux equal to 1 on the top edge of the left grid cell and 0 on all other grid edges. We proceed as follows:

$$\begin{aligned}
& \int_{\mathbf{U}_l} \mathbf{A}^{-1} \mathbf{w}(x, y) \cdot \mathbf{X}(x, y) dx dy \\
&= \int_{\mathbf{U}_l} \mathbf{w}(x, y) \cdot \mathbf{A}^{-T} \mathbf{X}(x, y) dx dy \\
&= \int_{\mathbf{U}_l} \|\mathbf{w}(x, y)\| (\mathbf{w}(x, y) / \|\mathbf{w}(x, y)\|) \cdot \mathbf{A}^{-T} \mathbf{X}(x, y) dx dy \\
&= \int_{\mathbf{U}_l} ((\mathbf{w}(x, y) \cdot \boldsymbol{\eta}_y(x, y)) / \sin(\theta(x, y))) \\
&\quad \cdot (\mathbf{Y}(x, y) / \|\mathbf{Y}(x, y)\|) \cdot \mathbf{A}^{-T} \mathbf{X}(x, y) dx dy \tag{3.14} \\
&= \int_0^1 \int_{\frac{1}{2}}^1 \hat{y} \mathbf{Y}(\hat{x}, \hat{y}) \cdot \mathbf{A}^{-T} \mathbf{X}(\hat{x}, \hat{y}) d\hat{x} d\hat{y} \\
&= \int_0^1 \int_{\frac{1}{2}}^1 \hat{x} \mathbf{A}^{-1} \mathbf{Y}(\hat{x}, \hat{y}) \cdot \mathbf{X}(\hat{x}, \hat{y}) d\hat{x} d\hat{y}.
\end{aligned}$$

The steps are the same as in the previous case except for step three, which uses equation (3.9) and the fact that \mathbf{w} and \mathbf{Y} are parallel. Again, the final integrand is a polynomial in the reference variables and can easily be evaluated analytically.

Note that for given \mathbf{A} , one could consider choosing the quadrilaterals such that $\mathbf{A}^{-1}\mathbf{Y} - \mathbf{X}$, making this integral vanish. This is unlikely to be useful in complex problems, but if \mathbf{A} is constant for example, it could be of interest.

Integrals for other basis functions can be evaluated in a manner similar to one of the two we presented here by a simple change of variables.

3.3 Using Fine Grid Integrals to Generate Coarse Grid Integrals

In this section, we will show how to generate coarse grid integrals from fine grid integrals, which is important when the permeability coefficient \mathbf{A} is piecewise constant on the fine grid cells but not on the coarse grid cells.

We begin by examining the relationship between fine and coarse grid finite element spaces. As mentioned in Section 2.2, the finite element spaces are nested; we will now make this statement more precise. In Figure 3.3, we depict a coarse grid volume \mathbf{P}_C and the four fine grid volumes $\mathbf{P}_i, i = 1, 2, 3, 4$, that are generated by bilinear refinement.

Letting \mathbf{W}_C denote the coarse grid velocity basis function with nonzero flux on the north edge of \mathbf{P}_C and similarly letting \mathbf{w}_i denote the fine grid velocity basis function with nonzero flux on the north edge on \mathbf{P}_i , we will prove the following result: within \mathbf{P}_C , we have

$$\mathbf{W}_C = \frac{1}{2}(\mathbf{w}_1 + \mathbf{w}_2) + \frac{1}{4}(\mathbf{w}_3 + \mathbf{w}_4). \quad (3.15)$$

We prove this result by verifying that this linear combination of fine grid

Figure 3.3: Coarse and Fine Volumes

basis functions has all of the properties that the coarse grid basis function is to have, namely:

- 1) The fluxes are zero on the east, south, and west edges of \mathbf{P}_C .
 - 2) The flux is one on the north edge of \mathbf{P}_C .
 - 3) The basis function is parallel to the vector field $\mathbf{Y}_C(x, y)$,
i.e., the basis function is aligned with the bilinear coordinates of \mathbf{P}_C
that correspond to vertical lines in the reference space.
 - 4) The quantity $\mathbf{W} \cdot \eta_y \|\mathbf{X}\|$ varies linearly with \hat{y} , and is constant
with \hat{x} , where all quantities are coarse grid quantities.
- (3.16)

The first property follows from the fact that each fine grid basis function, $\mathbf{w}_i, i = 1, 2, 3, 4$, has zero flux on the east, south, and west edges of \mathbf{P}_C . Thus the linear combination also has this property.

We now verify the second property in (3.16):

$$\begin{aligned} & \int_{\mathbf{P}_C^n} \left(\frac{1}{2} (\mathbf{w}_1 + \mathbf{w}_2) + \frac{1}{4} (\mathbf{w}_3 + \mathbf{w}_4) \right) \cdot \eta ds \\ &= \frac{1}{2} \int_{\mathbf{P}_1^n} (\mathbf{w}_1 \cdot \eta) ds + \frac{1}{2} \int_{\mathbf{P}_2^n} (\mathbf{w}_2 \cdot \eta) ds \\ &= \frac{1}{2}(1) + \frac{1}{2}(1) = 1. \end{aligned}$$

The first step follows from the fact that both \mathbf{w}_3 and \mathbf{w}_4 have zero flux on the north edge of \mathbf{P}_C , and the second step follows from the fact that both \mathbf{w}_1 and \mathbf{w}_2 have flux = 1 on the north edges of \mathbf{P}_1 and \mathbf{P}_2 , respectively.

The third property in (3.16) follows from the agreement of coarse and fine grid bilinear coordinates.

We are left with the fourth property in (3.16), to verify this, we will need the following result:

$$\text{If } (x, y) \in \mathbf{P}_i, \text{ then } \mathbf{X}_C(x, y) = 2\mathbf{X}_i(x, y). \quad (3.17)$$

Here, \mathbf{X}_C denotes the image of $(1,0)$ under the bilinear mapping from the reference space to \mathbf{P}_C , and \mathbf{X}_i denotes the image under the bilinear mapping from the reference space to \mathbf{P}_i . Result (3.17) follows directly from the fact that the fine grid cells are generated by bilinear refinement of the coarse grid cells. We can now verify the final property in (3.16). First consider any point along the upper dotted line in Figure 3.3. We evaluate:

$$\begin{aligned}
& \mathbf{W}_C(x, y) \cdot \eta_y^C(x, y) \|\mathbf{X}_C(x, y)\| \\
&= \left(\frac{1}{4} \mathbf{w}_3(x, y) + \frac{1}{2} \mathbf{w}_1(x, y) \right) \cdot \eta_y^1(x, y) (2 \|\mathbf{X}_1(x, y)\|) \\
&= \left(\frac{1}{2} \mathbf{w}_3(x, y) \cdot \eta_y^1 \right) \|\mathbf{X}_1(x, y)\| + (\mathbf{w}_1(x, y) \cdot \eta_y^1) \|\mathbf{X}_1(x, y)\| \\
&= \frac{1}{2} (1 - \hat{y}_1) + \hat{y}_1 = \frac{1}{2} + \frac{1}{2} \hat{y}_1 = \hat{y}_C.
\end{aligned} \tag{3.18}$$

Here we assumed that (x, y) was in \mathbf{P}_1 , but the result is the same if it is instead in \mathbf{P}_2 . In deriving this result, in the first step we used result (3.17), the fact the bilinear coordinates agree (thus, η_y is the same on both fine and coarse grids), and the fact that both \mathbf{w}_2 and \mathbf{w}_4 are zero within \mathbf{P}_1 . In the third step, we used the fact that

$$\mathbf{w} \cdot \eta_y \|\mathbf{X}\|$$

is linear in \hat{y} , where all variables are fine grid variables. If we now consider any point along the lower dotted line in Figure 3.3, we evaluate in a similar manner:

$$\begin{aligned}
& \mathbf{W}_C(x, y) \cdot \eta_y^C(x, y) \|\mathbf{X}_C(x, y)\| \\
&= \left(\frac{1}{4} \mathbf{w}_3(x, y) \cdot \eta_y^1(x, y) \right) 2 \|\mathbf{X}_1(x, y)\| \\
&= \frac{1}{2} \mathbf{w}_3(x, y) \cdot \eta_y^1 \|\mathbf{X}_1(x, y)\| = \frac{1}{2} \hat{y}_3 = \hat{y}_C.
\end{aligned} \tag{3.19}$$

In the above we assumed that (x, y) was in \mathbf{P}_3 , but the result is the same if it is instead in \mathbf{P}_4 . Results (3.18) and (3.19) together prove that the linear combination of fine grid basis function has the fourth property of (3.16). This completes the proof of result (3.15).

We now show how to use this result to generate coarse grid integrals from fine grid integrals. As an example, consider the discrete Darcy equation for the U volume that straddles the right edge of \mathbf{P}_C , again referring to Figure 3.3. In the assembling this equation, one must calculate the following integral:

$$\int_{P_2 \cup P_4} \mathbf{A}^{-1} \mathbf{W}_C(x, y) \cdot \mathbf{X}_C(x, y) dx dy,$$

where \mathbf{W}_C , say, is the coarse grid basis function with flux equal to 1 on the north edge of \mathbf{P}_C . Using the results:

within \mathbf{P}_2 :

$$\mathbf{W}_C = \frac{1}{4} \mathbf{w}_4 + \frac{1}{2} \mathbf{w}_2$$

$$\mathbf{X}_C = 2 \mathbf{X}_2$$

within \mathbf{P}_4 :

$$\mathbf{W}_C = \frac{1}{4} \mathbf{w}_4$$

$$\mathbf{X}_C = 2 \mathbf{X}_4$$

we can express the coarse grid integral in terms of fine grid integrals:

$$\begin{aligned}
& \int_{\mathbf{P}_2 \cup \mathbf{P}_4} \mathbf{A}^{-1} \mathbf{W}_C(x, y) \cdot \mathbf{X}_C(x, y) dx dy \\
&= \int_{\mathbf{P}_2} \mathbf{A}^{-1} \mathbf{W}_C(x, y) \cdot \mathbf{X}_C(x, y) dx dy \\
&+ \int_{\mathbf{P}_4} \mathbf{A}^{-1} \mathbf{W}_C(x, y) \cdot \mathbf{X}_C(x, y) dx dy \\
&= \frac{1}{2} \int_{\mathbf{P}_2} \mathbf{A}^{-1} \mathbf{w}_4(x, y) \cdot \mathbf{X}_2(x, y) dx dy \\
&+ \int_{\mathbf{P}_2} \mathbf{A}^{-1} \mathbf{w}_2(x, y) \cdot \mathbf{X}_2(x, y) dx dy \\
&+ \frac{1}{2} \int_{\mathbf{P}_4} \mathbf{A}^{-1} \mathbf{w}_4(x, y) \cdot \mathbf{X}_4(x, y) dx dy.
\end{aligned}$$

All of the integrals in the final result above are integrals that must be calculated to assemble the fine grid discrete Darcy equations. Thus, we need to calculate no new integrals to assemble the coarse grid Darcy equations. Further, if \mathbf{A} is piecewise constant on the fine grid but not on the coarse grid, this procedure allows us to calculate coarse grid integrals by, in essence, breaking the integral up into pieces where \mathbf{A} is constant.

4 Summary and Future Work

The mixed FVE discretization developed in here has been shown, through fairly exhaustive numerical testing, to produce high quality approximations for a wide variety of problems. On uniform grids, when the diffusion coefficient is discontinuous, the mixed FVE approach has been shown to produce significantly more accurate velocity approximations than those obtained from a standard cell-centered finite difference approach. Unlike standard cell-centered finite differences, the mixed FVE approach can also be applied in a clear and straightforward way to general quadrilateral grids and problems with full tensor permeability. Moreover, numerical experiments indicate that the approximations to the velocity retain their second-order convergence property in these more complicated applications.

The multilevel algorithms developed in this thesis have been shown, again through fairly exhaustive numerical testing, to provide an efficient method for solving the mixed FVE equations. Although the mixed FVE approach is somewhat more complicated than the standard finite difference approach, the multilevel methods solve the equations in work comparable to that needed

to solve the simpler finite difference equations. The connection between multigrid convergence factors and discretization errors is a major topic of reference [3]. With a poor discretization, i.e. the fine grid discrete problem is a poor approximation to the continuous problem, poor multigrid convergence often occurs. The reason is that a coarse grid discrete problem, coming from the same poor discretization process, is a poor approximation to the corresponding fine grid discrete problem, even in the smooth components. We certainly do not see poor multigrid convergence factors, and the good convergence factors that we do see are, to a degree, indicative of the good approximation properties of the mixed FVE discretization.

While the results of numerical tests for the mixed FVE approach are promising, it is our hope to verify them theoretically. In designing the method, we borrowed heavily from work done in mixed finite elements, where there are an abundance of theoretical results. Preliminary work has begun to put the mixed FVE method on a solid theoretical foundation. In particular, this early work has suggested a minor modification of the scheme which may yield super-convergence results for the pressure variable. A comparison, both numerically and theoretically, of the mixed FVE and mixed finite element approaches is also planned.

From a computational point of view, we plan to implement the mixed FVE scheme in more realistic applications, quite possibly in a working reservoir simulation code. Also, the mixed FVE approach, and the multilevel

algorithms for solving the equations, extend to three dimensions quite naturally, and a three-dimensional implementation of the scheme is currently being investigated.

Bibliography

- [1] R. E. Alcouffe, A. Brandt, J. E. Dendy, and J. W. Painter. The multi-grid methods for the diffusion equation with strongly discontinuous coefficients. *SIAM J. Sci. Stat. Comput.*, 2:430–454, 1981.
- [2] T. Arbogast, P. Keenan, M. Wheeler, and I. Yotov. Logically rectangular mixed methods for Darcy flow on general geometry. In *Proceedings of the 13th SPE Symposium on Reservoir Simulation*, pages 51–59, 1995.
- [3] A. Brandt. *Multigrid techniques: 1984 guide with applications to fluid dynamics*. GMD–Studien Nr. 85. Gesellschaft für Mathematik und Datenverarbeitung, St. Augustin, 1984.
- [4] A. Brandt, S. F. McCormick, and J. W. Ruge. Algebraic multigrid (AMG) for sparse matrix equations. In D. J. Evans, editor, *Sparsity and Its Applications*. Cambridge Univ. Press, Cambridge, 1984.
- [5] F. Brezzi and M. Fortin. *Mixed and Hybrid Finite Element Methods*, volume Number 15 of *Springer Series in Computational Mathematics*. Springer-Verlag, 1991.
- [6] W. L. Briggs. *A Multigrid Tutorial*. SIAM Books, Philadelphia, 1987.
- [7] Z. Cai, J. Mandel, and S. F. McCormick. The finite volume element method for diffusion equations on general triangulations. *SIAM J. Numer. Anal.*, 28:392–402, 1991.
- [8] J. E. Dendy. Black box multigrid. *J. Comput. Phys.*, 48:366–386, 1982.
- [9] J. E. Dendy, S. F. McCormick, J. W. Ruge, T. F. Russell, and S. Schaffer. Multigrid methods for three-dimensional petroleum reservoir simulation. In *Proceedings of the 10th SPE Symposium on Reservoir Simulation*, pages 19–25, 1989.

- [10] C. Duncan and J. Jones. A mixed method Poisson solver for three-dimensional self-gravitating astrophysical fluid dynamical systems. In N. D. Melson, T. A. Manteuffel, and S. F. McCormick, editors, *Sixth Copper Mountain Conference on Multigrid Methods*, volume CP 3224, pages 159–173, Hampton, VA, 1993. NASA.
- [11] R.E. Ewing and R.F. Heinemann. Incorporation of mixed finite element methods in compositional simulation for reduction of numerical dispersion. In *Proceedings of the 7th SPE Symposium on Reservoir Simulation*, pages 341–347, 1983.
- [12] R.E. Ewing, T.F. Russell, and M.F. Wheeler. Simulation of miscible displacement using mixed methods and a modified method of characteristics. In *Proceedings of the 7th SPE Symposium on Reservoir Simulation*, pages 71–81, 1983.
- [13] C. Liu and S.F. McCormick. The finite volume element method (FVE) for planar cavity flow. In *Proceedings of the 11th International Conference on CFD*, Williamsburg, VA, 1988.
- [14] S. F. McCormick. *Multilevel Adaptive Methods for Partial Differential Equations*, volume 6 of *Frontiers in Applied Mathematics*. SIAM Books, Philadelphia, 1989.
- [15] J. E. Morel, J. E. Dendy, M. Hall, and S. White. A cell-centered Lagrangian-mesh diffusion differencing scheme. *J. Comput. Phys.*, 103:286–299, 1992.
- [16] P.A. Raviart and J.M. Thomas. A mixed finite element method for 2nd order elliptic problems. In I. Galligani and E. Magenes, editors, *Mathematical Aspects of Finite Element Methods*, pages 292–315. Springer-Verlag, 1977.
- [17] T.F. Russell. Rigorous block-centered discretizations on irregular grids: Improved simulation of complex reservoir systems. Technical Report No. 2, Project Report, Reservoir Simulation Research Corporation, 1990.
- [18] T.F. Russell and M.F. Wheeler. Finite element and finite difference methods for continuous flows in porous media. In R.E. Ewing, editor, *The Mathematics of Reservoir Simulation*, pages 36–106. SIAM Books, 1983.
- [19] J.M. Thomas. *Sur l'analyse numerique des methodes d'elements finis hybrides et mixtes*. PhD thesis, à l'Université Pierre et Marie Curie, 1977.